Measuring stress-induced martensite microstructures using far-field high-energy diffraction microscopy

Ashley Nicole Bucsek,[a] Darren Dale,[b] Jun Young Peter Ko,[b] Yuriy Chumlyakov[c] and Aaron Paul Stebner[a]*

[a]Mechanical Engineering, Colorado School of Mines, 1610 Illinois Street, Golden, Colorado 80401, USA, [b]Cornell High Energy Synchrotron Source, 161 Wilson Laboratory Road, Ithaca, New York 14853, USA, and [c]Tomsk State University, 36 Lenin Avenue, Tomsk, 634050, Russian Federation. *Correspondence e-mail: astebner@mines.edu

Modern X-ray diffraction techniques are now allowing researchers to collect long-desired experimental verification data sets that are *in situ*, three-dimensional, on the same length scales as critical microstructures, and using bulk samples. These techniques need to be adapted for advanced material systems that undergo combinations of phase transformation, twinning and plasticity. One particular challenge addressed in this article is direct analysis of martensite phases in far-field high-energy diffraction microscopy experiments. Specifically, an algorithmic forward model approach is presented to analyze phase transformation and twinning data sets of shape memory alloys. In the present implementation of the algorithm, the crystallographic theory of martensite (CTM) is used to predict possible martensite microstructures (*i.e.* martensite orientations, twin mode, habit plane, twin plane and twin phase fractions) that could form from the parent austenite structure. This approach is successfully demonstrated on three single- and near-single-crystal NiTi samples where the fundamental assumptions of the CTM are not upheld. That is, the samples have elastically strained lattices, inclusions, precipitates, subgrains, R-phase transformation and/or are not an infinite plate. The results indicate that the CTM still provides structural solutions that match the experiments. However, the widely accepted maximum work criterion for predicting which solution of the CTM should be preferred by the material does not work in these cases. Hence, a more accurate model that can simulate these additional structural complexities can be used within the algorithm in the future to improve its performance for non-ideal materials.

1. Introduction

The desirable behaviors of many advanced alloys can be attributed to complex three-dimensional micromechanics including combinations of twinning, phase transformation and plasticity, all of which interact due to interface compatibility constraints. For example, the well known functional behaviors of shape memory alloys (SMAs) – superelasticity, shape memory effect and actuation – are enabled by a reversible, diffusionless solid-to-solid phase transformation from a high-temperature austenite phase to a low-temperature martensite phase (Duerig *et al.*, 1990; Otsuka & Wayman, 1998). These properties are further influenced by strong interactions with microstructure heterogeneities such as phase interfaces, stacking faults and grain boundaries, as well as precipitates, inclusions and plasticity resulting from processing (Otsuka & Ren, 2005). Pristine materials with microstructures composed solely of perfection-compatible interfaces are the exception (Chen *et al.*, 2013; Song *et al.*, 2013; Ni *et al.*, 2016). Improved understanding of these coupled, multidimensional micro-

mechanics is required for the continuing development of advanced alloys.
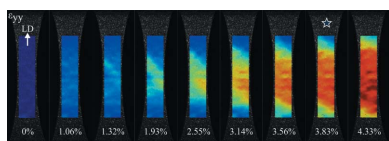
In the case of SMAs, fundamental micromechanical theory and modeling have been an active area of research for more than 70 years (Wechsler *et al.*, 1953; Bowles & Mackenzie, 1954; Bilby & Crocker, 1965). The crystallographic theory of martensite (CTM) (Wechsler *et al.*, 1953; Bilby & Crocker, 1965; Bowles & Mackenzie, 1954; Ball & James, 1987; Bhattacharya, 2003; Abeyaratne & Knowles, 1991; Hane & Shield, 1998) provides the foundation for our current understanding of SMA micromechanics (see Appendix *A*1 for SMA terminology definitions). However, this theory has fundamental assumptions: it ignores defects, precipitates, plasticity and strained lattices, and it assumes an infinite sample. Because of the challenge of providing direct experimental verification, the line between where the CTM assumptions apply and where they do not is still unclear, as is how to modify the theory for the cases where they do not. The lack of such experimental verification data can be attributed to several factors. First, the length scales of microstructure interfaces in an SMA routinely span 10 nm to 1 mm, making it difficult to use a single measurement technique to simultaneously observe all of the critical features during micro-

structure evolution (Li, 2002; Zhang *et al.*, 2000; Liu *et al.*, 1999, 2000; Inamura *et al.*, 2012; Nishida *et al.*, 1988, 2012; Coughlin *et al.*, 2012; Norfleet *et al.*, 2009). Second, most experimental techniques for observing microstructure evolution across the relevant length scales are limited to surface observations (Gall *et al.*, 2002; Kimiecik *et al.*, 2013, 2016; Laplanche *et al.*, 2017; Kim *et al.*, 2015; Shaw, 2000; Paul *et al.*, 2017) and typically cannot measure the out-of-plane deformations that result from these three-dimensional deformation mechanisms. Third, the three-dimensional measurement techniques that do exist are either destructive and prohibit *in situ* measurements (Hornbuckle *et al.*, 2015; Henrie *et al.*, 2005; Liu *et al.*, 2015) or are averaged over millions to billions of grains (Stebner *et al.*, 2013; Dunand *et al.*, 1996; Khalil-Allafi *et al.*, 2004; Šittner *et al.*, 2004; Šittner & Novák, 2004; Buhrer *et al.*, 1983).

With the introduction of high-brilliance synchrotron X-rays, a number of novel X-ray-based imaging and diffraction techniques have emerged that promise the ability to acquire the desired data sets. Collectively, these techniques can be used nondestructively to study *in situ* microstructure evolutions in three dimensions and across several length scales. Techniques for studying phenomena between 1 μm and 1 mm in length are well established, and more recent techniques currently in development now extend capabilities down to 100 nm (Simons *et al.*, 2015, 2016), with even higher magnifications on the horizon. In this work, we focus on one of the diffraction-based classes of these new techniques, which has been called three-dimensional X-ray diffraction (3DXRD), high-energy X-ray diffraction (HEXD) and high-energy X-ray diffraction microscopy (HEDM) (Poulsen *et al.*, 2001; Poulsen, 2004, 2012; Lauridsen *et al.*, 2001; Lienert *et al.*, 2011). More specifically, we use the far-field HEDM (ff-HEDM) technique, in which the X-ray detector is placed far away from the sample (∼1 m) relative to traditional diffraction configurations (see Appendix *A*2 for HEDM terminology and Appendix *B* for experimental setup details). This technique can be used to measure the grain-specific lattice (elastic) strain tensors, crystallographic orientations, centroid locations and volumes within bulk specimens (∼1 mm^3) all in three dimensions (Pagan & Miller, 2014; Miller & Dawson, 2014; Schuren *et al.*, 2015). Using this information, several long-standing questions can be answered, such as (i) what are the evolution pathways of different, often interacting deformation mechanisms?
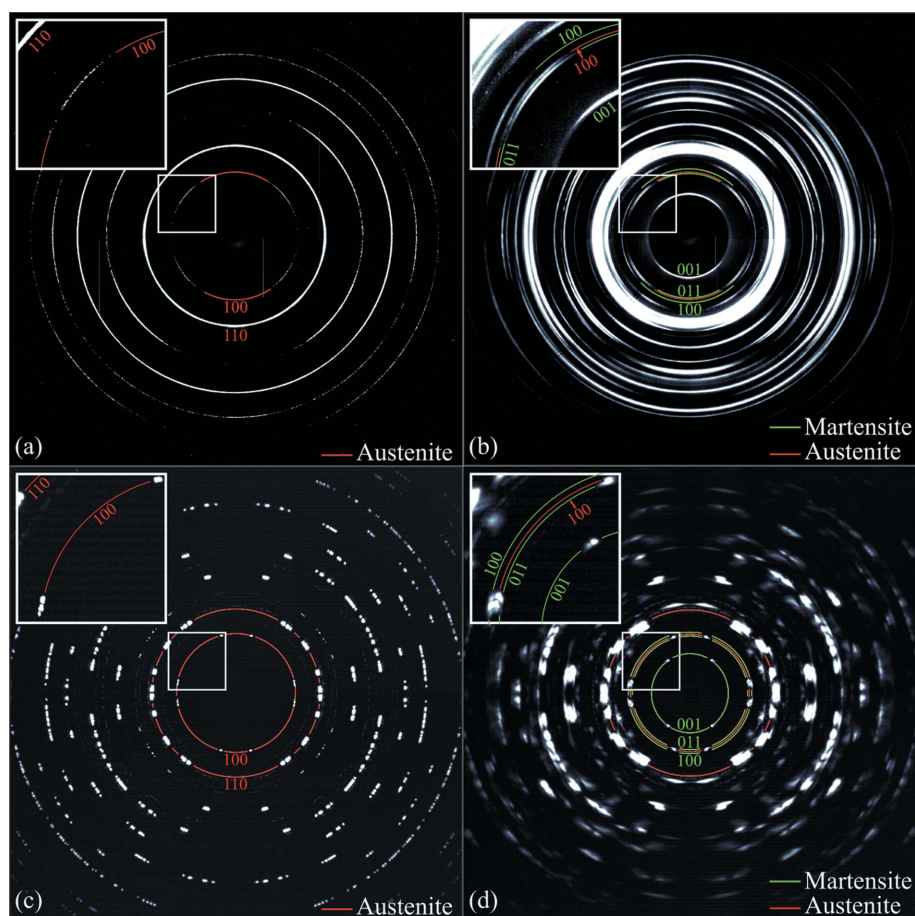

Figure 1
Summed ff-HEDM patterns for (*a*) an austenitic polycrystalline NiTi sample, (*b*) a partially transformed polycrystalline NiTi sample, (*c*) an austenitic single-crystal NiTi sample and (*d*) a partially transformed single-crystal NiTi sample. All patterns are summed over the full 360° of sample rotation.

(ii) how do existing micromechanical theories fare at predicting them? and (iii) what improvements can we make in how we use these micromechanical theories?

Researchers are already gaining novel insights into SMAs from ff-HEDM experiments. Using three-dimensional micrometre-scale studies, researchers were able to investigate the localized initiation and propagation of the transformation front in NiTi wires (Sedmák *et al.*, 2016), the pronounced rotation of austenite grains as a result of cycling through transformation (Berveiller *et al.*, 2011), and the heterogeneous stress response of austenite grains as a result of granular interaction and proximity to the surface (Paranjape *et al.*, 2017). To date, however, most insights gained from ff-HEDM data have been confined to direct studies of only the austenite phase.

The martensite phase presents unique challenges in analyzing ff-HEDM data, which relies upon the ability to uniquely separate and identify Bragg reflections from individual crystals in the sample. (i) The small domain sizes of the martensite phase can lead to size-effect broadening and overlapping Bragg reflections. (ii) The low symmetry of the martensite crystal structure leads to many low-structure-factor (hkl) rings (see Appendix $A2$ for a definition) that may start to overlap with each other and/or with the higher-symmetry austenite rings. (iii) Plasticity and/or elastic strains typically coincide with transformation events, also causing broadening (*e.g.* Paranjape *et al.*, 2018; Pagan & Miller, 2014). These signatures convolute when the effects occur simultaneously, thereby making it difficult to identify individual reflections or even separate (hkl) rings. Fig. 1(a) shows the summed ff-HEDM pattern from an austenitic NiTi polycrystal that is ideal for ff-HEDM analysis with distinct, high-intensity reflections that are well separated (see inset). Fig. 1(b) shows the summed ff-HEDM pattern of the same sample after it has partially transformed, resulting in a powder-like pattern that is unideal for ff-HEDM. The complication of the diffraction pattern for ff-HEDM analysis is present even for initially austenite single-crystal samples, as shown in Figs. 1(c), 1(d) where distinct, high-intensity austenite reflections (Fig. 1c) partially transform to diffuse, overlapping, low-intensity martensite reflections situated very close to austenite reflections and to other martensite reflections (Fig. 1d).

After documenting the materials and measurements used in this work in §§2.1–2.2, a forward model algorithm to analyze the microstructures (*i.e.* martensite orientations, twin mode, habit plane, twin plane and twin phase fractions) of SMA martensite phases in ff-HEDM data sets is presented (§2.3 and Appendix $C1$), enabling the quantification of stress-induced transformation modes and other related micromechanics (see Appendix $A1$ for SMA terminology). This approach utilizes the fact that in most ff-HEDM analyses of SMAs, although the martensite phase cannot be directly quantified on a crystal-by-crystal basis, the austenite phase can. If the initial austenite microstructure is known, then all of the possible martensite microstructures can be predicted using known relationships given by the CTM. The diffraction patterns of the possible martensite microstructures are then simulated and compared with the experimentally measured diffraction patterns [*i.e.* forward modeled (Wong *et al.*, 2013; Pagan & Miller, 2014)], and the observed martensite microstructures are identified by the closest statistical comparison between the simulated and experimental patterns. The comparisons are performed on unit pole figures, which isolate the orientation information within HEDM data; these pole figures can also be used to determine orientation distribution functions within crystals, such as in the work of Barton & Bernier (2012), where researchers used a pole figure to study the $\alpha \rightarrow \varepsilon$ phase transition in iron. We validate this approach in §3 by applying it to three single- and near-single-crystal NiTi ff-HEDM data sets of martensite microstructures.

To apply this approach to future polycrystalline data sets like that of Fig. 1(b), a method for ranking the likelihood of each martensite microstructure is desired to accelerate the algorithm and to improve the statistical probability of finding the right answer. For example, a NiTi polycrystal with n illuminated grains will have 192^n possible stress-induced microstructures assuming one twin system per grain. This would likely result in an undetermined system when hundreds of grains are considered simultaneously, especially considering that several twin systems may form within each grain, further increasing the statistical ambiguity if all possible solutions are considered. Hence, in §3.5, we also present an investigation of using a widely accepted analytic model for this purpose: the maximum transformation work criterion (Bhattacharya, 2003; Zhang *et al.*, 2000; Chu, 1993; Shield, 1995) (see Appendix A and Appendix $C2.4$). This model states that the transformation system that produces the most mechanical work is the most likely to form, providing a simple and straightforward ranking method for the probability of martensite microstructures to form during phase transformation, just as Schmid factor calculations provide a simple, analytic model for predicting the probabilities of slip systems to activate during plastic deformation. This aspect of the article builds from the work of previous researchers (Lind *et al.*, 2014; Abdolvand *et al.*, 2015) who used HEDM results to test the Schmid ranking of twinning systems in zirconium polycrystals.

The discussion in §4.1 focuses on what worked well in these initial applications of the algorithm; namely, martensite microstructure solutions provided by the CTM were found to be in good agreement with experiments. §4.2 documents why, in spite of the successes in using the CTM to identify the martensite microstructure solutions, the use of the maximum transformation work criterion to rank the likelihoods of those solutions was unsuccessful. §§4.3–4.5 then evaluate possible strategies for improving the statistical rankings of the CTM solutions, including accounting for the elastic strain of the austenite grains just before transformation. In addition to summarizing the key points, the conclusion in §5 also suggests other approaches for improvement for more complex data, such as using full-field micromechanical models within the algorithm.

Finally, it is recommended that readers unfamiliar with SMAs first review the SMA terminology we use in this work
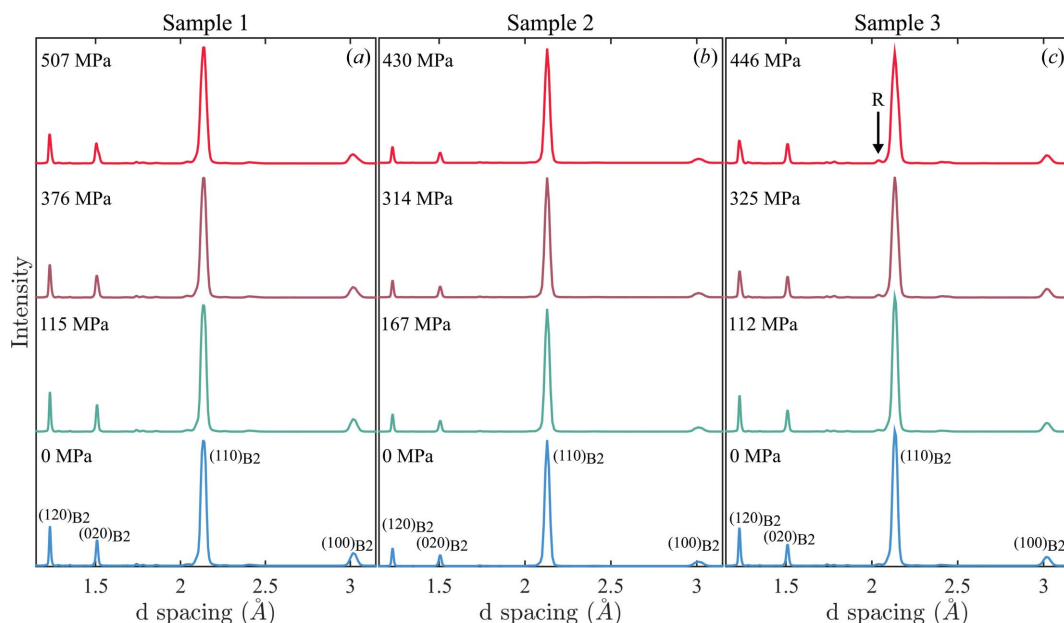
Figure 2
Integrated intensity *versus* *d*-spacing line profiles for (*a*) sample 1, (*b*) sample 2 and (*c*) sample 3 at incremental load steps in the primarily elastic loading regime.

(Appendix *A*1) and those unfamiliar with ff-HEDM first review the HEDM terminology (Appendix *A*2), as well as the experimental approach overview (Appendix *B*). Appendix *C* documents the details of the calculations and is recommended for those readers who want to use and/or modify the algorithm.

2. Materials and methods

2.1. Sample preparation and initial microstructures

The three samples were electrical-discharge-machined (EDM) from a 40 mm-diameter near-single-crystal $Ni_{50.6}Ti_{49.4}$ ingot. The ingot was grown by an advanced Bridgman technique consisting of remelting a cast ingot into a graphite crucible under an inert helium gas atmosphere. The material was found to have TiO_2/TiC inclusions and Ni_4Ti_3 precipitates – the microstructure is documented in greater detail by

Paranjape *et al.* (2018). Aside from these secondary phases, the samples are B2 cubic austenite at room temperature (see 0 MPa load diffraction patterns in Fig. 2).

The specimen geometry, shown in Fig. 3, consists of a 1 mm^2 gauge cross section with 1 mm gauge length. At the energies typically used for ff-HEDM experiments (*i.e.* 50–80 keV), X-rays can transmit through 1–2 mm of most metals, including NiTi (the maximum path length for X-rays through a 1 mm square cross section is 1.41 mm). This specimen geometry was modified from that used by Turner *et al.* (2016) to reduce the gauge section length to 1 mm and add compression shoulders. These modifications were made to ensure that the phase transformation occurred within the diffracted volume, which is 1 mm tall in this work, and to allow for tension–compression reversed loading (though we do not use the latter feature in this work). Samples 1 and 2 were cut parallel to the ingot axis, and sample 3 was cut with its axis 30° from the ingot axis. The
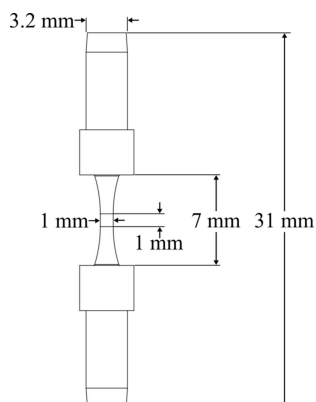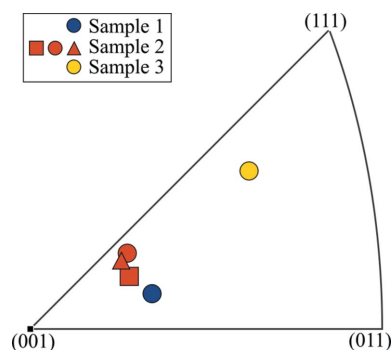

Figure 3
Square gauge specimen geometry.

Figure 4
Initial austenite (B2) orientations for all three samples shown in an equal area projection inverse pole figure (IPF) with respect to the loading axis.

Table 1
Austenite (B2) plasticity Schmid factors corresponding to the orientations plotted in Fig. 4.

	Sample 1	Sample 2			Sample 3
		Subgrain 1	Subgrain 2	Subgrain 3	
m	0.23	0.23	0.25	0.23	0.46

orientations for all three samples are shown in Fig. 4. The B2 orientations were measured using the *MIDAS* ff-HEDM analysis suite (Sharma *et al.*, 2016). Note that sample 2 was found to have three austenite subgrains in the diffracted volume of the gauge section. The plasticity Schmid factors, m, associated with these orientations are provided in Table 1.

2.2. ff-HEDM measurements and loading

The loading and *in situ* ff-HEDM measurements were performed at the F2 beamline at the Cornell High Energy Synchrotron Source (CHESS). The loading was performed on the RAMS2 load frame (Shade *et al.*, 2015). The samples were quasi-statically loaded in tension in displacement control to induce transformation while periodically fixing the crosshead in displacement to take ff-HEDM measurements. As discussed in Appendix *B*, the ff-HEDM technique requires that the sample be rotated while being held in the load frame. In our particular experiment, the load train of the RAMS2 load frame was on air bearings and could rotate continuously (rather than the whole load frame being on a rotation stage). At user-defined points in the loading, the loading was paused and the specimen was rotated while maintaining the load using a servomotor, gear reducer, preloaded linear ball spline and two timing belts [see Shade *et al.* (2015), Schuren *et al.* (2015) for more details]. When the loading was paused for ff-HEDM measurements, the detector data were binned at 0.1° incre-

Figure 5
Stress–strain curves for the three single-crystal NiTi samples loaded in tension to induce transformation. The stars mark the load steps that were selected for ff-HEDM analysis.

ments for a full 360° rotation, resulting in 3600 recorded detector images. A dark image for background subtraction was collected at each load step.

The X-ray beam was collimated to 1 mm tall × 2 mm wide for all measurements. The detector was a GE41RT amorphous silicon area detector with 2048 × 2048 pixels and 200 × 200 µm pixel size. The detector calibration parameters (*i.e.* sample-to-detector distance, detector center, detector tilt and detector distortion) were obtained from a CeO_2 powder sample using *MIDAS*. The monochromatic X-ray beam energy and sample-to-detector distance were 55.618 keV and 1012 mm for samples 1 and 3, and 61.332 keV and 797 mm for sample 2. To measure the macroscopic strain, the optical features contrasted directly from the EDM finish (*i.e.* no speckle pattern was applied) were recorded with an FLIR (Point Gray) Grasshopper GS3-U3-50S5M-C camera with a Sony ICX625 2448 × 2048 (2/3″) CCD with 3.45 µm pixel size and a Standard & Precision Optics (SPO) TCL0.8X-110-HR lens with a 110 mm working distance, 14.9 µm resolution and 0.0255 numeric aperture. The displacement fields and strains were calculated from these images using *Ncorr* digital image correlation (DIC) software (Blaber *et al.*, 2015) using a subset radius of 15 pixels and a subset spacing of 2 pixels. The analyses reported strain values with a strain noise of $\pm 4 \times 10^{-4}$. Only the data collected from the 1 mm-tall, 1 mm-wide gauge section surface area that faced the camera during loading were used to calculate the macroscopic strains for the mechanical responses given in Fig. 5. The reported values are the mean values over the gauge face.

2.3. Forward modeling algorithm

A detailed description of the forward modeling algorithm is provided in Appendix *C*1 and shown in Fig. 14. The virtual diffractometer portion of the algorithm was constructed following the procedure outlined by Pagan & Miller (2014), Bernier *et al.* (2011). The algorithm can be summarized as follows. (i) The initial austenite microstructure [crystal orientation(s), lattice parameters] is measured using traditional ff-HEDM software such as *FABLE* (Gotz *et al.*, 2007), *HEXRD* (Bernier *et al.*, 2011) or *MIDAS* (Sharma *et al.*, 2016). (ii) The austenite information is used to construct a list of possible martensite microstructure predictions using the CTM. (iii) Each possible martensite orientation is forward modeled using the same laboratory conditions as the actual experiment. Because these samples are near-single crystals the samples were centered on the rotation axis, the martensite orientations were simulated from the center of the virtual sample and all perturbations introduced by precession were assumed to be small enough to be ignored. (iv) The virtual diffraction patterns are compared with the experimental diffraction patterns, and the closest agreement of virtual and measured diffraction patterns is used to determine the martensite microstructures. In this work, we considered the Bragg reflections in the three innermost monoclinic B19′ (hkl) rings: $(001)_{B19'}$, $(011)_{B19'}$ and $(100)_{B19'}$ (see Fig. 1d). These (hkl) rings are sufficiently high-intensity and relatively well separated in
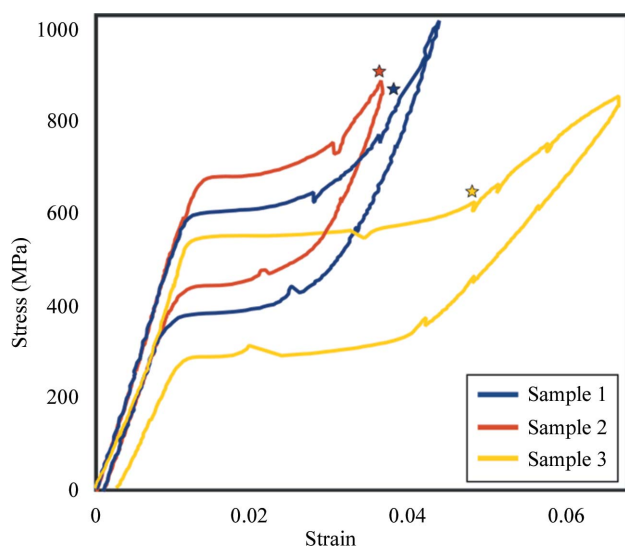
research papers

2θ from other B2 and B19$'$ (*hkl*) rings. There were a total of 32 reflections per twin, or habit plane variant (HPV) (see Appendix *C*2.3) within these three (*hkl*) rings. For these 32 reflections, we used summed and normalized Euclidean distances between the reflections produced by the virtual diffractometer (VD) and the experimental diffractometer (ED), $\parallel \text{VD} - \text{ED} \parallel$, on a unit pole figure (see Appendix *C*1). The results were used to construct a ranked table, in which the highest-ranked HPV solution is the one with the smallest $\parallel \text{VD} - \text{ED} \parallel$. In the case in which two HPV solutions had effectively identical $\parallel \text{VD} - \text{ED} \parallel$, the twin volume fraction f was used as a final criterion.

Because these are single-crystal samples that produced a small number of martensite orientations during phase transformation, the martensite reflections could be deconvoluted from the austenite reflections *via* manual inspection. Specifically, the detector images for each rotation increment were stacked vertically, and the pixels exceeding a baseline intensity threshold were plotted with 50% transparency, creating a three-dimensional visualization of the reflections. Overlapping B2 and B19$'$ reflections were separated by 2θ, and

Figure 6
Frames showing the longitudinal Lagrangian strain ε_{YY} from the DIC analysis for (*a*) sample 1, (*b*) sample 2 and (*c*) sample 3. The macroscopic strain corresponding to each frame is labeled underneath it and a star is placed on the frames that correspond to the load steps selected for ff-HEDM analysis.

overlapping B19$'$ reflections were separated by identifying maxima separated in η and ω. Finally, the centroids of the individual reflections were calculated based on the reflection intensity maxima. The intensity maxima may have some noise associated with them, especially due to the combination of the disparity in orientation volumes and the dynamic range of the detector. In general, a more sophisticated technique may be applied such as a batch processing algorithm to deconvolute close or overlapping reflections using image processing or statistical algorithms (Sharma *et al.*, 2016). For samples with hundreds to thousands of grains that become very powder-like upon transformation, this approach can be modified to compare developing martensite textures on a volume basis.

3. Results

3.1. Mechanical responses and *in situ* diffraction data

All three stress–strain curves are shown in Fig. 5, and the sequences of frames from the DIC analysis showing the Lagrangian strain in the loading direction between no load
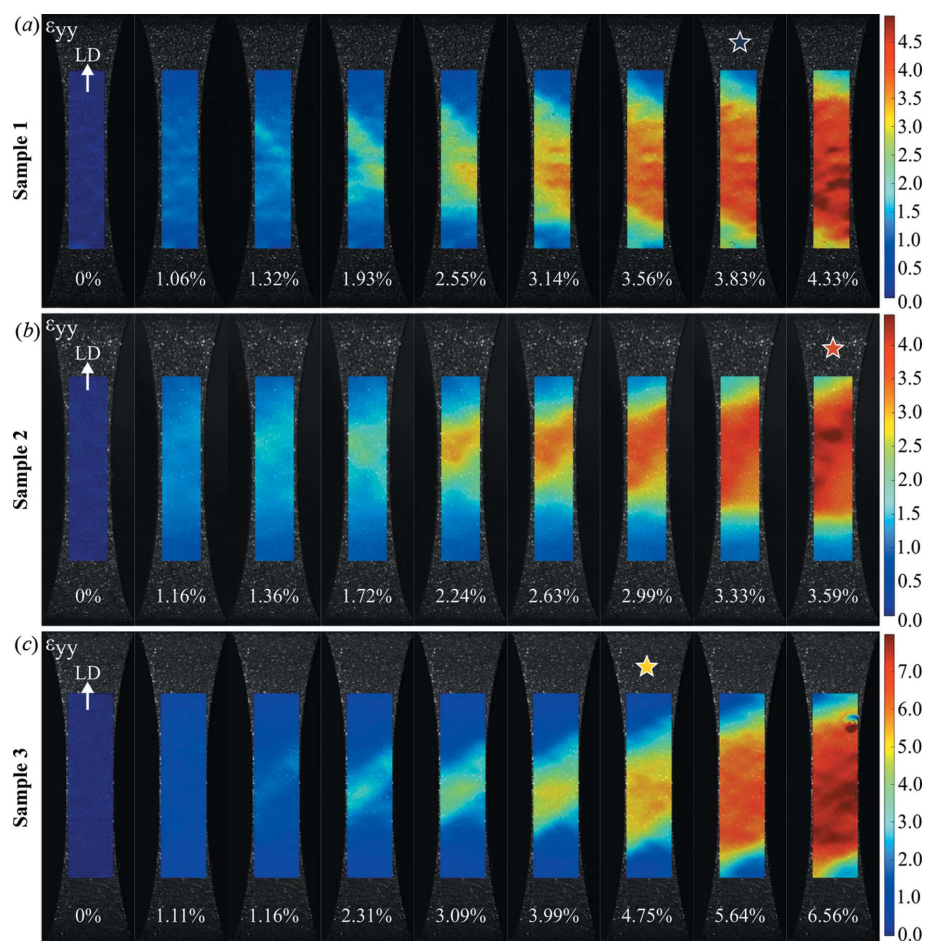
and peak load are shown in Fig. 6. Note that, while strains outside of the gauge sections are shown in Fig. 6 to give a complete visualization of the surface deformations, the macroscopic strain values plotted in Fig. 5 are the mean strain only from the 1 mm-tall, 1 mm-wide gauge section portions of the analyzed regions (see §2.2). Stress relaxation can be seen at many but not all of the points where we paused to take ff-HEDM measurements in Fig. 5. The star markers in Figs. 5 and 6 indicate the load steps that correlate with the ff-HEDM diffraction data collected under load that are presented in this article. These points were chosen for two reasons: (i) the martensite volumes are large enough to produce reflections with high intensities; (ii) additional microstructure changes due to plasticity can be largely avoided (although the interaction between transformation and plasticity is of some interest, the purpose of this work is to identify martensite microstructures).

Fig. 7 shows the sequences of summed ff-HEDM patterns during the transformation plateau for samples 1 (Fig. 7*a*), 2 (Fig. 7*b*) and 3 (Fig. 7*c*). Only a quarter slice of the detector is shown given the symmetry of the diffraction pattern [*e.g.* Fig. 1(*d*) illustrates the quarter slice region of interest for sample

Table 2
Summary of results for samples 1–3.

	Sample 1	Sample 2	Sample 3
Macroscopic strain in loading direction before transformation plateau, ε^e	1.12%	1.27%	1.16%
Maximum strain in loading direction at load step of interest, ε^*	4.35%	4.32%	5.58%
Transformation strain in loading direction at load step of interest, $\varepsilon^{\mathrm{transf}} = \varepsilon^* - \varepsilon^e$	3.23%	3.05%	4.42%
Fraction of B2 transformed to B19′ at load step of interest, λ^*	0.82	0.70	0.79

2]. Fig. 7 shows that the twins that formed upon transformation initiation were the only twins that formed during loading (within the resolution capabilities of the technique).

Shown in Table 2 are the macroscopic strains before the transformation plateau ε^e, the maximum strains (within the illuminated volume) at the load steps of interest ε^*, the transformation strain at the load steps of interest estimated by $\varepsilon^{\mathrm{transf}} = \varepsilon^* - \varepsilon^e$, and the fractions of the austenite that transformed to martensite (within the illuminated volume) at the load steps of interest λ^*. These fractions were calculated by comparing the B2 (hkl) ring intensities before loading and at the load steps of interest. All strain values are the Lagrangian strains in the loading direction.

With respect to Fig. 5, the seemingly elastic region of the mechanical response exhibited by sample 3 deviates from those exhibited by samples 1 and 2 after about 0.15%. In NiTi SMAs, this type of nonlinear elastic behavior well before the transformation plateau is usually indicative of an intermediate R-phase transformation. To investigate the emergence of R-

phase, we looked at the integrated intensity *versus* d-spacing line profiles at different load steps within the elastic (or seemingly elastic) regions, shown in Fig. 2. The small peak to the left of the highest-intensity (110) B2 peak at a d spacing of ~2.1 Å could possibly be the (202, 022) reflections of R-phase or the (312, 4−12) and/or (051) reflections of Ni_4Ti_3 precipitates. However, this peak is absent in the structure of sample 3 at 0 MPa (Fig. 2c), only appearing under load and being most pronounced at 446 MPa. Because Ni_4Ti_3 precipitates do not grow during loading at room temperature, this result implies a partial transformation from B2 to R-phase in sample 3 prior to the B19′ transformation plateau. The illuminated volumes of samples 1 and 2 did not exhibit an R-phase transformation that could be detected with this technique.

3.2. Initial measurements needed for algorithm inputs

The B2 crystal orientation measurements (Fig. 4) together with the B2 and B19′ lattice parameters are required inputs to the analysis algorithm (Fig. 14). The initial B2 lattice parameters and the average B19′ lattice parameters as described by monoclinic symmetry, measured using the *MIDAS* ff-HEDM analysis suite (Sharma *et al.*, 2016), are shown for each sample in Table 3. Table 3 also shows the experimental twin fractions f, where f is applied to the minor correspondence variant (CV) i in a twin pair $i–j$ [see equation (7) in Appendix C]. The twin fractions were calculated in the following way. For each (hkl) ring, some reflections would be of relatively low intensity (corresponding to the minor CV reflections), some reflections would be of relatively high intensity (corre-
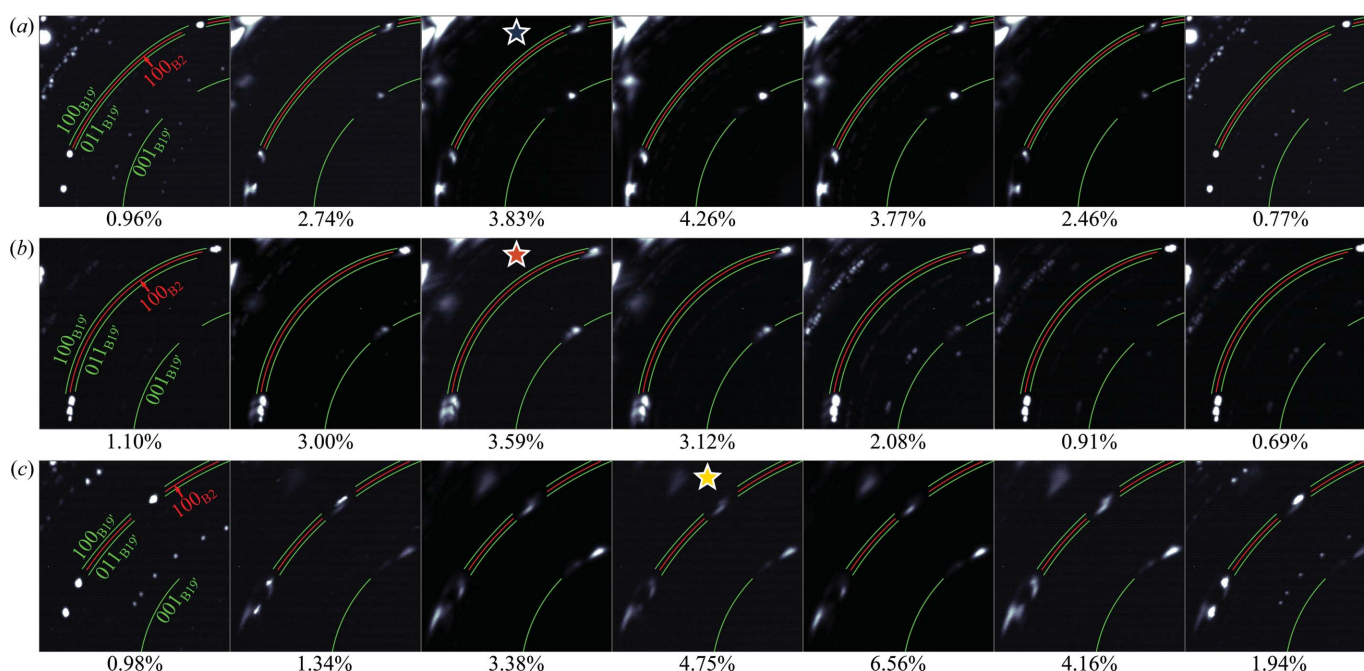

Figure 7
Sequences of the summed ff-HEDM patterns for samples 1 (*a*), 2 (*b*) and 3 (*c*) marked with the macroscopic strain values at which the ff-HEDM data were collected. A star is placed on the frames that correspond to the load steps selected for the analysis. All patterns are summed over the full 360° of sample rotation. The sections of the patterns used in this figure take advantage of the fourfold symmetry of the summed diffraction pattern, illustrated in Fig. 1(*d*).

Table 3
Initial B2 lattice parameters and average B19′ lattice parameters, as well as twin fractions of the minor CV in the unidentified martensite twins at the load steps of interest.

Sample		a_0	a	b	c	β	Twin fraction, f
1		3.011	2.914	4.137	4.580	97.12°	0.09
2	Subgrain 1	3.008	2.902	4.141	4.582	97.11°	0.28
	Subgrain 2	3.009					
	Subgrain 3	3.009					
3		3.001	2.923	4.104	4.593	97.00°	0.25

Table 4
Normalized macroscopic and crystal stress components.

		$\sigma_{11}/\|\sigma\|$	$\sigma_{22}/\|\sigma\|$	$\sigma_{33}/\|\sigma\|$	$\sigma_{23}/\|\sigma\|$	$\sigma_{13}/\|\sigma\|$	$\sigma_{12}/\|\sigma\|$
Macroscopic for all three samples		0	1	0	0	0	0
Crystal for sample 1		0.346	0.878	0.309	−0.008	0.002	0.121
Crystal for sample 2	Subgrain 1	0.077	0.983	0.090	0.073	0.054	0.104
	Subgrain 2	0.135	0.968	0.169	0.073	0.050	0.088
	Subgrain 3	0.092	0.985	0.064	0.059	0.050	0.109

Table 5
Identified HPV solutions.

Sample	1	2	3	
HPV type	10−4 I(−)	9−1 I(−)	3−11 I(+)	3−11 II(−)
Twin plane, $\hat{\mathbf{n}}_{B2}$	{110}	{110}	{110}	{4.010 1.000 1.000}
Shear vector, $\mathbf{a}_{B2}$	{0.272 0.099 0.068}	{0.270 0.106 0.075}	{0.285 0.091 0.059}	{0.216 0.206 0.020}
Habit plane, $\hat{\mathbf{m}}_{B2}$	{0.870 0.490 0.046}	{0.867 0.696 0.047}	{0.835 0.547 0.062}	{0.928 0.358 0.104}
Shape strain vector, $\mathbf{b}_{B2}$	{0.095 0.049 0.028}	{0.095 0.061 0.031}	{0.096 0.041 0.025}	{0.099 0.044 0.000}

sponding to the major CV reflections). The twin phase fractions were measured by comparing the intensities of the lower-intensity martensite reflections with those of the higher-intensity martensite reflections.

As discussed in §1, we are also interested in testing the effectiveness of using the maximum transformation work criterion to predict the most preferred and therefore most likely martensite microstructures. As discussed in Appendix C2.4, the crystal stress state is needed to calculate the transformation work. The stress states that should be used are the cubic elastic stresses within the elastic loading regime just before any transformation initiates that might result in relaxation. For comparison, we used both the macroscopic stress state as well as the crystal (grain-averaged) stress states. The macroscopic stress state is uniaxial tension in $\hat{\mathbf{Y}}_L$ (as defined in Fig. 13). The full crystal lattice strain tensors were measured using *MIDAS* and the crystal stress states were then calculated assuming the elastic constants published by Mercier *et al.* (1980). The root-mean-square (RMS) strain errors for the measurements reported by *MIDAS* were 0.05% for sample 1 and 0.14%, 0.15% and 0.13% for the three subgrains for sample 2. The normalized macroscopic and crystal stress states within the elastic loading regime are provided in Table 4 (written in the laboratory coordinate system shown in Fig. 13). The grain-averaged, unrelaxed elastic stress state for sample 3 could not be measured because of the early partial R-phase transformation, so only the macroscopic stress state was used for this sample.

3.3. Identified martensite microstructures

The identified HPVs for all three samples are shown in Table 5 (see Appendix C2 for definition of the notation). Experimental observations of the {110} HPV types have previously been reported by Gupta & Johnson (1973), Onda *et al.* (1992), Madangopal & Banerjee (1992), Otsuka *et al.* (1971), and others. For sample 2, all three subgrains were found to form the same HPV, so only the solution for subgrain 2 is shown. For sample 3, two HPVs, 3−11 I(+) and 3−11 II(−), were found to be present in the experimental data, with the former having a larger overall volume fraction.

As mentioned in §2.3, the HPVs given in Table 5 were statistically selected by the algorithm as the HPVs with the virtual diffraction pattern that produced the smallest $\| VD - ED \|$ (again, the error between the VD and the ED patterns). The twin fraction f was used as the deciding criterion when multiple solutions resulted in the same $\| VD - ED \|$. For example, considering sample 1, the martensite orientations for inverse HPV pairs 10−4 I(−) and 4−10 I(−) are almost identical: thus, the $\| VD - ED \|$ for these inverse HPV pairs will be effectively identical. ('Inverse HPVs' are used here to mean the same twin types composed of the same CVs, where the minor and major CVs are switched.) The only difference is whether the twin fraction f favors CV 10 or CV 4. The relative favoring of one variant or the other is directly observable from the diffraction data, as described in §3.2 and given in Table 3. The experimental f

Table 6
Theoretical twin fractions *f* and theoretical transformation twinning strains.

Also included for comparison are the experimental twin fractions (reprinted from Table 3) and the experimental transformation strains (reprinted from Table 2).

Sample	HPV	Theoretical twin fraction	Experimental twin fraction	Theoretical transformation strain	Experimental transformation strain
1	10−4 I(−)	0.29	0.09	3.21%	3.23%
2	9−1 I(−)	0.29	0.28	2.64%	3.05%
3	3−11 I(+)	0.31	0.25	1.57%	4.42%

values are listed again in Table 6 next to the theoretical *f* values for the sake of more direct comparison. This result will be further discussed in §3.5.

3.4. Virtual *versus* experimental diffraction patterns

The virtual reflections of the HPVs are plotted on top of the experimental diffraction patterns in Fig. 8. Only the first three B19′ (*hkl*) rings are shown, and only a quarter slice of the detector is shown given the symmetry of the diffraction pattern [*e.g.* Fig. 1(*d*) illustrates the quarter slice region of interest for sample 2]. The solution shown for sample 2 (Fig. 8*b*) is for subgrain 2, but the other solutions are effectively identical. The insets show close-ups of the regions marked by white boxes. In Fig. 8(*c*), the virtual reflections of the HPV 3−11 II(−) are shown, and in Fig. 8(*d*), the virtual reflections of the HPV 3−11 I(+) are shown. While both

Table 7
Work ranking for samples 1, 2 and 3 using both the macroscopic stress state and the crystal stress state.

Sample	HPV	Maximum work ranking using macroscopic stress	Maximum work ranking using crystal stress
1	10−4 I(−)	28	48
2	9−1 I(−)	38	49
3	3−11 I(+)	56	−

systems appear to be present, the HPV 3−11 I(+) in Fig. 8(*d*) has a much larger overall volume fraction. The larger volume fraction of this HPV is illustrated by the large, bright (100) reflection in the lower-left corner, which corresponds only to this HPV in Fig. 8(*d*).

3.5. Maximum work criterion

Table 7 shows the ranking of each solution according to the maximum work criterion using the macroscopic stress state (third column) and grain-averaged crystal stress state (fourth column). The first-ranked HPV would have produced the maximum work and the last-ranked would have produced the minimum work (for example, if the HPV that formed in sample 1 has a ranking of 28, then that HPV produced the 28th largest work compared with all 192 HPVs that could have formed in sample 1). The calculations for these values are provided in Appendix *C*2.4. For both the macroscopic and the crystal stress states, the ranking is closest to ideal (ideal being a ranking of 1) for sample 1, which is a B2 single crystal with inclusions and precipitates. The ranking is lower for sample 2, which differs from sample 1 by having subgrains. Finally, the ranking is lowest for sample 3 [using the high-volume 3−11 I(+) HPV], which differs from samples 1 and 2 by having a large tendency for plasticity and exhibiting an intermediate R-phase transformation.

In Fig. 9, ‖ VD − ED ‖ *versus* work is plotted for all 192 possible HPVs for all three samples. In Figs. 9(*a*), 9(*c*), 9(*e*) the macroscopic stress state was used to calculate work, and in Figs. 9(*b*), 9(*d*) the grain-averaged crystal stress state was used to calculate work. For all three samples, the eight HPVs with the lowest ‖ VD − ED ‖ values belong to the same CVs. For example, for sample 1 (Figs. 9*a*, 9*b*), the eight HPVs with the lowest ‖ VD − ED ‖ values are all of the 10−4 or 4−10 HPVs [*i.e.* 4−10 I(−), 4−10 I(+), 4−10 II(−), 4−10 II(+), 10−4 I(−), 10−4 I(+), 10−4 II(−) and 10−4 II(+)]. This demonstrates the
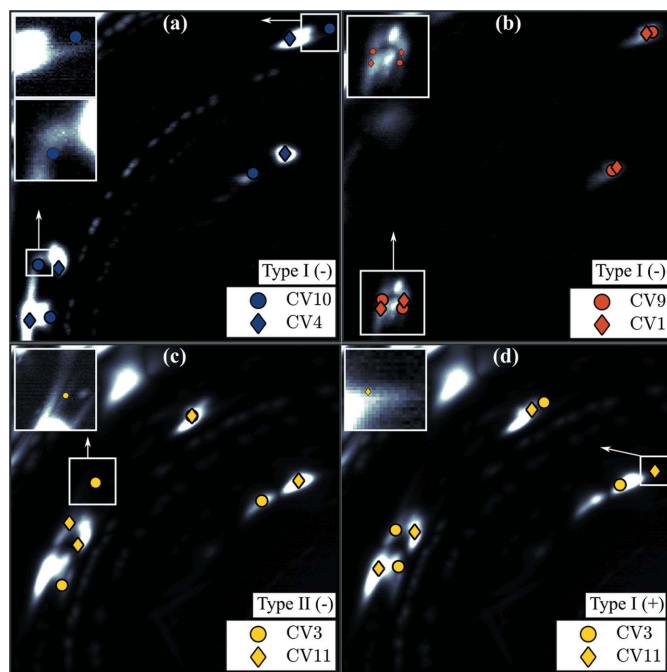
Figure 8
The virtual reflections are plotted on top of the experimental diffraction patterns for the identified HPVs for samples 1 (*a*), 2 (*b*) and 3 (*c*), (*d*). Two HPV solutions are shown for sample 3, because both HPV solutions are present. All patterns are summed over the full 360° of sample rotation. The sections of the patterns used in this figure take advantage of the fourfold symmetry of the summed diffraction pattern, illustrated in Fig. 1(*d*).

robustness of the algorithm in identifying present CVs for future cases in which this may be the only measurement of interest. All other CV pair types have substantially larger $\| VD - ED \|$ values. The closeness of the solutions for inverse HPVs are pointed out for each sample in the insets [*e.g.* HPVs 9−1 I(−) and 1−9 I(−) in Fig. 9(*c*)], reaffirming
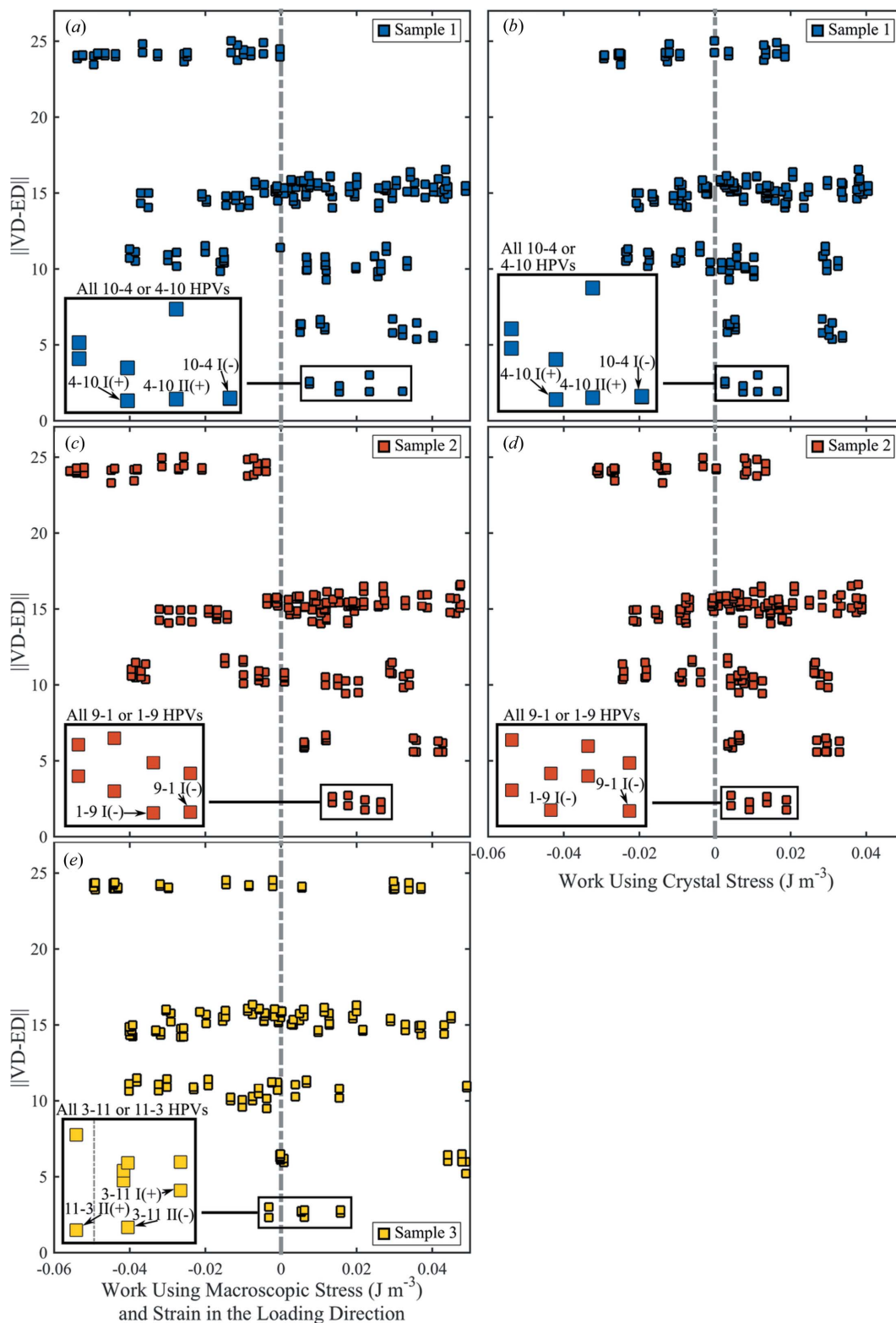

Figure 9
$\| VD - ED \|$ *versus* work for all 192 HPV solutions using the macroscopic stress state to calculate work for sample 1 (*a*), sample 2 (*c*) and sample 3 (*e*) and using the crystal stress states to calculate work for sample 1 (*b*) and sample 2 (*d*). In the cases where the macroscopic stress state was used, the work is equivalent to the strain in the loading direction.

the need to incorporate twin fractions as a final solution criterion.

4. Discussion

4.1. The CTM provides martensite microstructure solutions that match experiments, even for materials that do not meet the assumptions of the CTM

The identified HPVs given in Table 5 and discussed throughout §3 have been largely validated with the following supporting evidence. (i) The error between the virtual and experimental diffraction patterns, $\| VD - ED \|$, is small (Fig. 9), hence the experimental and virtual diffraction patterns are in very good quantitative and qualitative agreement (Fig. 8). (ii) The predicted twin fractions and the experimentally observed twin fractions agree (Table 6). The experimental twin fraction for sample 1 is unusually low, so the discrepancy between the experimental and theoretical twin fractions for sample 1 could be due to the dynamic range of the detector and the attenuation setting during this particular test. (iii) The theoretical and experimental transformation twinning strains agree (Table 6). Sample 3 drastically underestimates the transformation strain for both the strained and unstrained case, but this is not surprising as this sample also exhibited an R-phase transformation, substantial plastic deformation and additional transformation modes that were not measured in our analyses. (Fig. 10 highlights some low-intensity reflections that were not included in the procedure.) (iv) The more theoretically favorable HPVs, according to the maximum work criterion, produce virtual diffraction patterns that are far from the experimental diffraction patterns (i.e. have large $\| VD - ED \|$ values) (Fig. 9).

This study has validated the CTM-based forward model algorithmic approach to identify stress-induced martensite microstructures in single- and near-single-crystal ff-HEDM

Figure 10
Low-intensity reflections not included in the analysis that likely belong to other low-volume-fraction HPVs in sample 3.

data sets, even when these samples do not adhere to the assumptions of the CTM (i.e. defect-free, strain-free, no finite boundaries such as grain boundaries or free surfaces). This demonstration was a necessary first step to applying the same approach to polycrystalline ff-HEDM data sets. However, our results also indicate that further advancements are needed to evaluate martensite in polycrystalline data sets. For example, the solution for sample 3 was optimized based on the assumption of one HPV, but there were at least two HPVs present. As shown in Fig. 10, there may also be additional low-volume-fraction twins present in sample 3 that are not accounted for by the two solutions shown in Figs. 8(c), 8(d). In this work, the two HPV solutions for sample 3 were manually identified, but the presence of multiple HPVs forming in one grain demonstrates a need to automate the selection process to include cases where more than one HPV forms and/or when reorientation events occur. One way to do this in the future is to estimate the number of HPVs (or combinations of HPVs and CVs in the case of reorientation) using the number of experimental martensite reflections, and then use combinations of HPVs in the forward model virtual versus experimental diffraction pattern statistical comparison.

Another current challenge in applying this procedure to polycrystalline data sets is in the hardware used for the experiments. More specifically, the limited dynamic range of existing detectors makes it difficult to simultaneously analyze microstructures that have features with both large and small diffracting volumes. Setting attenuation levels low enough to measure the reflections of the small-volume features will cause the reflections of the large-volume features to saturate the detector, while setting the attenuation such that the reflections of the large-volume features do not saturate will cause the reflections of the small-volume features to fall into the detector background noise. This limitation is also why most studies of polycrystals strive for grains of similar size with a low standard deviation (Sedmák et al., 2016; Paranjape et al., 2017), why it is challenging to observe fine twins within large grains of Mg and other alloys (Aydiner et al., 2009), why observing transformation nucleation events is not possible, and why it is difficult to measure all transformation microstructures.

Realistically, transforming polycrystalline data sets will produce powder patterns like the one shown in Fig. 1(b), where the many martensite reflections are low in intensity relative to the austenite reflections and highly overlapping. In these cases, the virtual and experimental patterns will need to be compared on a texture basis using statistical analyses; textures are much easier to measure than individual grains in the cases of diffuse, low-intensity, overlapping reflections. Similarly, it will not be possible to measure the martensite lattice parameters through ff-HEDM analysis suites in these cases. For these future cases, the average B19′ lattice parameters may be measured using a traditional lattice parameter refinement approach at the onset of transformation. Again, one will need to consider combinations of HPVs and the possibility of multiple HPVs per grain, likely resulting in an
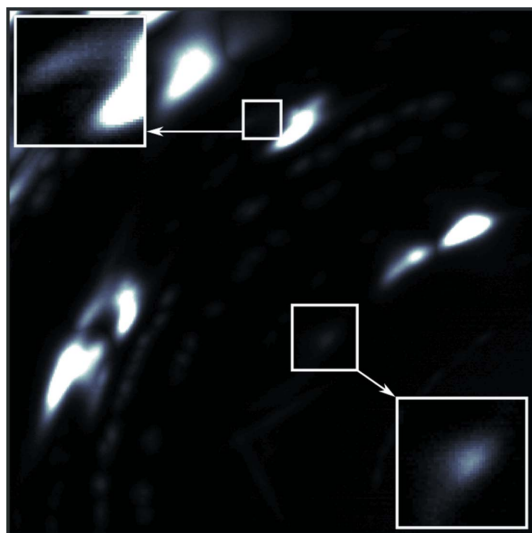
undetermined system. To address this issue, we used this initial validation of the algorithmic approach to evaluate the efficacy of using the maximum transformation work criterion to reduce the number of possible HPVs, discussed in the next section.

4.2. The maximum transformation work criterion only ranks the probabilities of martensite microstructures for materials that exactly meet the assumptions of the CTM

Consistent with the previous report on sample 2 by Paranjape *et al.* (2018), the HPV that would have produced the largest mechanical work under tension did not form in sample 2. In fact, we find that the HPV that would have produced the largest mechanical work did not form for any of the three single-crystal samples explored in this article. None of the solutions even have strain rankings in the top ten out of 192 formed, which is even more significant considering that many of the 192 solutions actually produce compressive transformation strains under tensile load (*i.e.* are physically implausible). Considering that Miyazaki *et al.* (1984) performed experiments on NiTi crystals that satisfied the fundamental assumptions of the CTM and found that the maximum transformation work criterion did accurately rank the most probable martensite microstructure in those samples, it is nearly certain that the reason the model did not work for these experiments is due to deviations from the fundamental assumptions of the CTM. All three samples have precipitates and inclusions, and are not an infinite plate. Additionally, in all three samples the martensite is forming from strained austenite, where the CTM assumes strain-free interfaces.

Most interestingly, it appears that there may be a hierarchy of assumption violations. Sample 1, which is a B2 single crystal with a low Schmid factor (for slip) but contains Ni_4Ti_3 precipitates along with carbide and/or oxide inclusions, most closely met the predictions of the maximum work criterion (Table 7). Sample 2 differed from sample 1 by having three low-angle misoriented subgrains, and in this case the maximum work criterion rankings performed worse. Sample 3 differed from sample 1 by having a high Schmid factor (for slip) and an intermediate R-phase transition, and in this case the maximum work criterion rankings performed worse yet.

These results illustrate that materials deviating from the underlying assumptions of the CTM will affect the ability to predict transformation modes using the CTM + maximum work criterion. They also suggest that more assumption deviations will lead to poorer performance of the model, which is expected. It is possible that modifying the CTM + maximum work criterion framework to model the real microstructure complexities could still result in an analytic framework that can be used for more complex materials. The remaining discussion points of this article may help direct future studies in this regard. Another option is to resort to forward modeling through full-field models of the microstructures, as was shown in a parallel work (Paranjape *et al.*, 2018) and is commonly used for plasticity (Wong *et al.*, 2013; Pagan & Miller, 2014; Obstalecki *et al.*, 2014). However, the latter option greatly increases the required computation, and

at the full-field scale, phenomena such as twinning are still very difficult to model accurately across many length scales, as they present themselves in SMAs. So further development is needed either way.

4.3. Preferential shearing mechanisms could provide a crystallographic means to rank preferred HPVs

There is one possibly revealing similarity between the identified HPVs that formed in each sample. From the pole figures in Fig. 11, it can be seen that the identified HPVs formed so that the $\{011\}_{B19'}$ and $\{100\}_{B19'}$ directions are closely aligned with the $\{001\}_{B2}$-type directions. This is not necessarily unique to these HPVs. What is unique, however, is how the $\{011\}_{B19'}$ poles sheared away from the $\{001\}_{B2}$ poles. For all three samples, the $\{011\}_{B19'}$ poles are rotated away from the $\{001\}_{B2}$ poles about the loading axis (Y). This is especially clear for the $(010)_{B2}$ poles, which is the B2 $\{001\}_{B2}$-type pole most aligned with the loading direction. That is, a CV i $\{011\}_{B19'}$-type pole and a CV j $\{011\}_{B19'}$-type pole are arranged on either side of the $(010)_{B2}$ poles, rotated about the loading direction. This did not occur for any of the higher-ranked HPVs for any of the three samples. In effect, the $\{011\}_{B19'}$ poles are shearing away from the $\{001\}_{B2}$ poles so that new $\{011\}_{B19'}$ poles remain, on average, in the same direction as the $\{001\}_{B2}$ poles. This tendency to maintain the average pole directions could be a

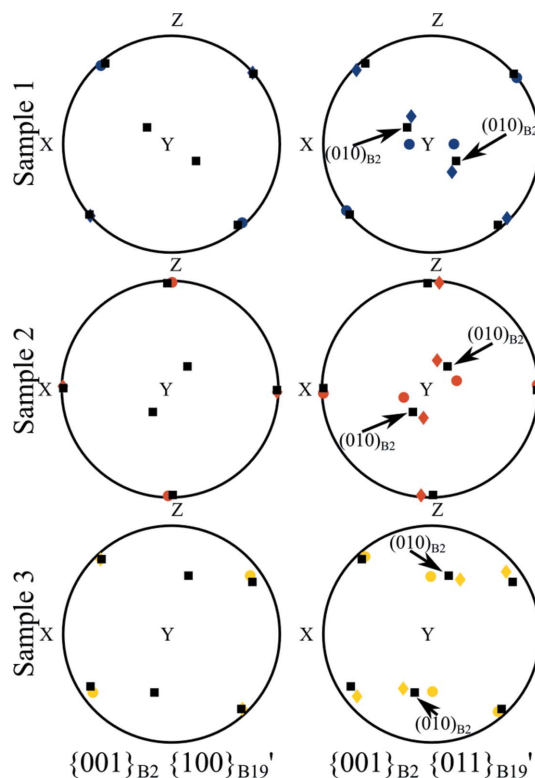**Figure 11**
The initial $\{001\}_{B2}$ poles and the $\{100\}_{B19'}$ and $\{011\}_{B19'}$ poles from the identified HPVs for each sample. The B2 poles are black squares and the B19' poles are colored circles (CV i) and diamonds (CV j) according to the same designations as in Fig. 8. All pole figures are equal area projections.

way to minimize distortion between the transformed lattice and the untransformed lattice, or it could be an effect of the constraint that the loading is placing on the lattice. This is simply an observation at this time and would require a larger number of samples to substantiate.

4.4. Using strained *versus* unstrained B2 lattice parameters will change the predictions made using the CTM

A fundamental assumption of the CTM is that making the calculations using unstrained lattice parameters properly predicts the HPVs that will form. In superelasticity and actuation behaviors, however, strained martensite forms from strained austenite. To our knowledge, calculations for incorporating strained lattice parameters into the existing CTM framework have not been previously reported. The CTM calculations for cubic-to-monoclinic transitions outlined in Appendix C2 are based on the crystal symmetry relationships between the B2 and B19′ point groups. An elastically strained lattice will not maintain this crystal symmetry except in the case of hydrostatic loading. Thus, the prediction of HPVs that are geometrically compatible during superelastic transformations requires a modified CTM framework in which both the austenite and martensite crystal lattices can take on arbitrary

(triclinic) symmetries due to elastic strains. Deriving this theory is beyond the scope of the current work, though such theory could easily be inserted into the 'CTM Calculations' box of the algorithm procedure shown in Fig. 14.

The work of Miyazaki *et al.* (1984) suggests that perhaps strain does not matter, since in their case they found the preferred HPVs formed from strained austenite. Here, we make one easy check towards evaluating if that is a generally applicable result, or just circumstance. We assume that the B2 lattice is hydrostatically strained at the time of transformation, thereby maintaining the B2 crystal symmetry and the existing cubic-to-monoclinic CTM framework. We study if this presence of hydrostatic strain can alter the predictions of HPVs. While the samples in our experiments are not hydrostatically strained, it is possible that in a polycrystal, a grain could predominantly experience hydrostatic strain, or that the local strain state at a stress concentration could be approximately hydrostatic. In any case, this analysis provides a general evaluation of the effect of strain on CTM predictions before making the recommendation to consider strains that break symmetry and requiring derivations of the CTM equations for triclinic-to-triclinic cases.

The boundary conditions for the strains we considered in this simple analysis were inspired from the DIC analysis frames of the three experiments just before the onset of the transformation plateau, *i.e.* frames corresponding to macroscopic strains of 1.06% for sample 1, 1.16% for sample 2 and 1.11% for sample 3 in Fig. 6. While these macroscopic strains just before transformation are ~1%, larger local strains (~1.5%) were observed in the DIC frames. Considering that regions either embedded within the sample volume or below the spatial resolution of the DIC analysis could have exhibited even larger strains, we evaluate up to 2% strains for this study. We also evaluate strains in compression to account for the possible local strain states influenced by precipitates and inclusions (see Paranjape *et al.*, 2018).

Fig. 12 shows the effects of varying the B2 lattice parameter a_0 between −2 and 2% on $\|\text{VD} - \text{ED}\|$, twin phase fraction and transformation strain. Figs. 12(a)–12(c) show the results for sample 1. The same HPV solution (given in Table 5) was found to minimize the error between the virtual and experimental diffraction patterns, $\|\text{VD} - \text{ED}\|$, for all values of a_0, but this HPV solution produced virtual diffraction patterns that were variably closer to or farther from the experimental diffraction pattern
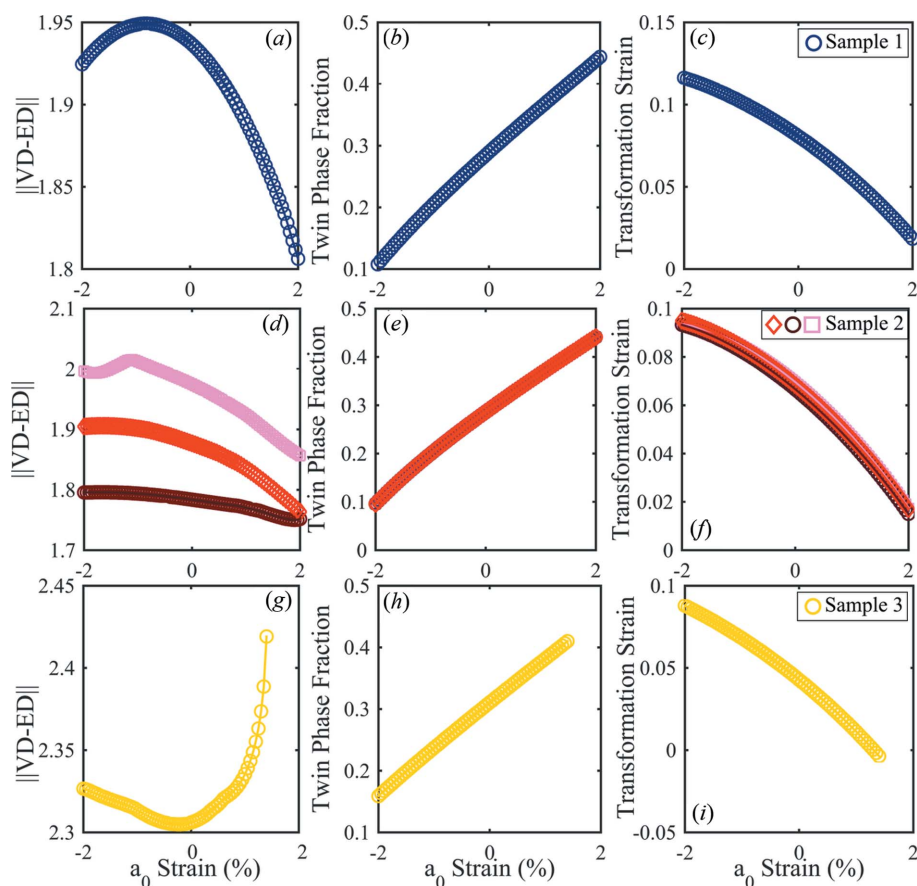

Figure 12
Effects of varying the input B2 lattice parameter between −2 and 2%. The $\|\text{VD} - \text{ED}\|$ versus a_0 strain is shown in (a), (d), (g), the theoretical twin fraction, f, versus a_0 strain is shown in (b), (e), (h), and the theoretical transformation twinning strain (in the loading direction) versus a_0 is shown in (c), (f), (i).

depending on whether an unstrained or strained a_0 was used (Fig. 12*a*). The corresponding twin phase fractions (Fig. 12*b*) and transformation strains (Fig. 12*c*) for this HPV also varied greatly depending on whether an unstrained or a strained a_0 value was used. The same dependence on the a_0 strain is demonstrated for sample 2 (Figs. 12*d*–12*f*) and sample 3 (Figs. 12*g*–12*i*). Note that the HPV solution that minimized ‖ VD − ED ‖ changed only for sample 2, subgrain 3 [see the 'kink' in Fig. 12(*d*)], and HPV solutions do not exist for strains larger than 1.4% for sample 3 (Figs. 12*g*–12*i*), *i.e.* transformation is not possible.

As a first exploration of the effect of using strained lattice parameters to make HPV predictions using the CTM, this study considered a hydrostatically strained austenite lattice in order to maintain the symmetries underlying the cubic-to-monoclinic framework of the CTM. Although the lattices in these three samples were not hydrostatically strained (except for perhaps at local strain states influenced by precipitates and inclusions), this study demonstrates how using strained *versus* unstrained lattice parameters as inputs to the CTM will have significant effects on the HPV predictions.

4.5. Using local stress heterogeneities instead of grain-averaged stress states may improve the CTM + maximum work criterion analytical model

Paranjape *et al.* (2018) showed how local stress heterogeneities at inclusions can serve as initiation sites for transformation much like a notch on the sample surface. Consider a hypothetical case where a specific HPV initiates at a stress concentration at an inclusion. In cases where it costs less energy for the initiated HPV to propagate than for additional HPVs to nucleate, the HPV that initiates at the stress concentration at this inclusion will propagate throughout the grain until it has fully transformed. This inclusion can be thought of as a 'critical microstructure feature', because it dictates the deformation process and therefore the overall response of the grain. Some of the microstructure features that violate the underlying assumptions of the CTM and are present in these three samples (inclusions, precipitates, grain boundaries, plasticity and R-phase) may be acting as critical microstructure features. In these cases, the maximum work criterion could more accurately predict the most likely HPV if the local stress state of the critical microstructure feature was known and used instead of the grain-averaged stress state. Therefore, the framework of using the CTM + maximum work criterion may be significantly improved by incorporating, for example, an Eshelby-type calculation for stress concentrations based on the microstructure features observed in the material. Implementing this modification to the forward model algorithm will cost more computationally than the current version, but not as much as a full-field microstructural model such as the one used by Paranjape *et al.* (2018). Furthermore, this modification may save computational power for polycrystalline data sets by drastically reducing the number of microstructures that need to be forward modeled.

5. Conclusion

A forward model for identifying martensite microstructures from ff-HEDM data sets was presented and verified on bulk NiTi single-crystal samples in the presence of precipitates and inclusions, subgrains, R-phase, plasticity and strain. Using this approach, the HPVs that formed under stress were identified for all three samples with a search space narrowed by using the CTM. The results showed that the CTM can reliably be used to make HPV predictions even for materials that do not necessarily meet the assumptions of the CTM. The results also showed that there is much room for improvement in the application of the maximum transformation work criterion for materials that do not meet the assumptions of the CTM. Suggestions for improvements include considering preferential shearing mechanisms, developing a new triclinic-based framework for the CTM where elastic distortions of the crystal structures can be incorporated, and using local stress concentrations at precipitates, inclusions, grain boundaries and other 'critical microstructure features' instead of the grain-averaged stress states. This need for improvement demonstrates the utility of these three-dimensional, *in situ*, bulk specimen data sets to shed light on our existing micromechanical theories and lead us towards greater capabilities in modeling and prediction of complex material systems.

This forward model approach is a necessary step in adapting novel diffraction techniques to advanced alloys that may exhibit phase transformation and twinning. These are, after all, the materials research areas most in need of the three-dimensional, microscale experimental data sets. We have used the version of the CTM-based forward model approach presented in this article to measure the HPVs (*i.e.* martensite orientations, habit plane, twin plane and twin phase fractions), an approach which can be immediately applied to martensitic transformations in steels, ceramics and minerals. To measure other interesting microstructure features such as twin fineness and local strain heterogeneities, the forward model procedure outlined in this article can be augmented. One interesting augmentation would be to combine it with a sophisticated microstructure model such as phase field modeling as done by Paranjape *et al.* (2016). The simulated microstructure from the phase field model would replace the boxes between 'Martensite Lattice Parameters' and 'Virtual Diffractometer' in the User Input sequence in the algorithm flowchart shown in Fig. 14, and each voxel from the simulated microstructure would be forward modeled. This could be incorporated with a machine learning feedback loop that used comparisons between the virtual diffraction pattern from the simulated microstructure and the experimental diffraction pattern to improve the simulation parameters.

This research marks the first step in adapting the powerful diffraction techniques being developed to complex phase-transforming and twinning material systems. The types of algorithmic approaches demonstrated in this article combined with the necessary advancements in microstructure prediction will lead to experimental data sets that are *in situ*, three-dimensional and on the length scale of the critical micro-

structure features, and are strongly needed for the development of fundamental micromechanical theory and modeling of advanced materials.

APPENDIX *A*
Terminology

A1. Shape memory alloy terminology

Refer to Bhattacharya (2003) for further reading.

Correspondence variant (CV). Because of the symmetry disparity between the austenite phase and the martensite phase, the martensite can form in several unique orientations of crystals relative to an austenite orientation. These are called correspondence variants (CVs), or simply 'variants'. In NiTi, there are 12 possible martensite CVs, as the cubic austenite crystal structure has 24 symmetry rotations, while the monoclinic martensite crystal structure has 2, and 24/2 = 12. The number of variants that can form in a martensitic transformation can be similarly calculated through the ratio of symmetries of the austenite and martensite point groups for other materials.

Crystallographic theory of martensite (CTM). Also called the phenomenological theory of martensite or the theory of martensite crystallography, the CTM is a continuum model for calculating allowable microstructures that arise from martensitic transformations. This theory is based upon the lattice shapes, sizes and orientation relationships between the austenite and martensite phases and restricts the allowable microstructures that can form *via* transformation to those that satisfy or approximate geometric compatibility (also called 'kinematic compatibility' or just 'compatibility' in the open literature), *i.e.* how the lattices from the two phases are able to fit together sharing a common plane of undistorted atoms.

Habit plane. The crystallographic plane that defines the interface between the austenite and martensite phases.

Habit plane variant (HPV). Because the austenite and martensite phases in NiTi (and most other SMAs) are not perfectly geometrically compatible, the martensite will form in twins of pairs of CVs, each with a very specific volume fraction, in order to approximate geometric compatibility at the austenite–martensite interface in an average sense. The most compatible martensite twin morphologies are calculated using the CTM and these structures are called habit plane variants (HPVs). There are 192 theoretically possible HPVs in NiTi.

Martensitic transformation. A solid-to-solid phase transformation between a high-symmetry phase and a low-symmetry phase. In NiTi, the high-symmetry, high-temperature phase is called austenite and it is a B2 cubic phase. The low-symmetry, low-temperature phase is called martensite and it is a B19′ phase. A martensitic transformation is defined by the fact that the movements of the individual atoms are diffusionless and the resultant lattice deformation is homogeneous (*i.e.* the atom movements are coordinated). The defining characteristic of SMAs is that the martensitic transformations are thermoelastic, where they are not in other materials.

Maximum transformation work criterion. A criterion commonly used to predict which HPV will form as a result of stress-induced transformation. This criterion states that the HPV that produces the most mechanical work when formed from the parent austenite crystal is the most likely.

Stress-induced transformation. Martensitic transformation can be induced by loading an SMA when it is in the austenite phase and the temperature is above but relatively close to the critical temperature for transformation. When the load is released, the material will return to the austenite phase. This is called stress-induced transformation, or superelastic loading.

Transformation modes. This is a general term for the different possible martensite microstructures that can form as a result of transformation. It is analogous to a slip mode in plasticity. In this article, it refers to the HPVs that can form as a result of stress-induced transformation.

Transformation strain. In this article, the transformation strain, or transformation twinning strain, is the macroscopic strain due to an austenite crystal (partially) transforming to a martensite twin, or HPV. This strain is typically less than the local, microstructural transformation strain from one part of the austenite crystal transforming to one martensite CV, because it is the weighted average of the strain contributions from the two CVs that compose the HPV, where the strains are weighted by the twin phase fractions.

A2. Far-field high-energy diffraction microscopy terminology

Refer to Poulsen (2004) for further reading.

Bragg condition. The condition for the X-rays scattered by atoms to constructively interfere when the atoms are arranged in some kind of periodic fashion (*e.g.* in a lattice).

Bragg reflections. When the Bragg condition for a plane of atoms is met, the X-rays scattered by the atoms will constructively interfere in two particular directions. When these directions intersect the plane of an X-ray detector, the detector measures the intensity distributions of the X-rays. These intensity distributions are called Bragg reflections.

Diffraction pattern. When a sample is illuminated by an X-ray beam, the (*hkl*) planes inside the sample that are in the Bragg condition will diffract. That is, the X-rays scattered by the atoms in these planes will constructively interfere. When the diffracted X-rays intersect the plane of an X-ray detector, the detector will record the intensity distributions of the diffracted X-rays. This two-dimensional detector measurement is called a diffraction pattern.

Far-field high-energy diffraction microscopy (ff-HEDM). The detector is placed far from the sample (on the order of 1 m). The reciprocal-space distribution of lattice strains and orientation dominate the diffraction pattern, and quantities like grain-averaged lattice strains, orientation and volume can be resolved.

Forward model. Creating virtual or simulated diffraction patterns of a virtual microstructure using the same laboratory parameters as an actual experiment including rotation direction and increment, detector size, detector pixel size, detector calibration parameters and X-ray energy.

High-energy diffraction microscopy (HEDM). A diffraction-based technique where the sample is illuminated by high-energy (50–100 keV), high-brilliance monochromatic X-rays. The sample is rotated about an axis perpendicular to the X-ray beam direction and diffraction patterns are collected in some user-defined rotation increment (every 0.1°, 0.25° or 0.5°). The series of diffraction images collected over each full rotation of the sample is then analyzed using vector calculus, and the resulting data can be used to visualize the microstructure of the sample in three dimensions, which leads to the use of the term 'microscopy'.

(hkl) rings. In ff-HEDM, the Bragg reflections of planes with equal inter-planar spacings, or d spacings, will lie in a circle on the detector called a Debye–Scherrer ring. Because planes of equal d spacing correspond in crystallography to (hkl) families, we call these rings (hkl) rings.

Summed diffraction pattern. In the case of HEDM, a diffraction pattern is recorded every rotation increment. For ease of representation, these individual diffraction patterns can be aggregated into a summed diffraction pattern. Typically, the summed diffraction pattern shows the maximum intensity at each pixel; it can also show the average intensity or total intensity at each pixel.

Virtual diffractometer. A virtual microstructure is diffracted through a virtual diffractometer, which is the name for the entire computational system of simulating the diffraction patterns using the same laboratory parameters as an experiment.

APPENDIX B
High-energy diffraction microscopy technique

A schematic of the ff-HEDM experimental setup is shown in Fig. 13. The laboratory coordinate system $\{X, Y, Z\}_L$ is defined by the incoming X-ray beam and the rotation axis. The test specimen may be a single crystal or polycrystal. Each crystal is described in its own crystal coordinate system $\{X, Y, Z\}_C$, defined by the crystal orientation. The test specimen is placed in the path of the incoming X-ray beam ($-Z_L$) on a 360° rotation stage that rotates in ω about an axis perpendicular to the incoming X-ray beam (Y_L). Along each rotation increment $\Delta\omega$, the integrated diffraction pattern is recorded by the detector, producing $360°/\Delta\omega$ images. Each Bragg reflection can then be defined in the detector's Cartesian coordinate system in $\{X, Y\}_D$ or in a polar coordinate system in $\{2\theta, \eta, \omega\}$. In other words, even though ω refers to the rotation of the test specimen, it can be used in the data
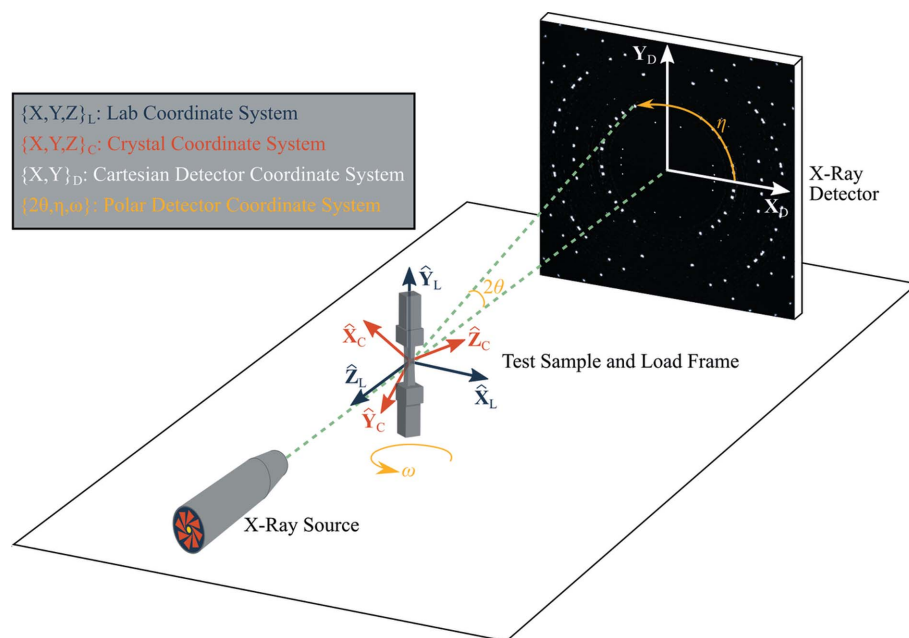

Figure 13
A schematic of the ff-HEDM experimental setup showing the relations between the pertinent coordinate systems. Sample gauge thicknesses for the HEDM technique are typically 0.5–2 mm, depending on the X-ray energy and the sample material attenuation and grain sizes, as discussed in §2.1.

processing to add a third spatial dimension to the detected data. The diffraction intensity is the measured signal in this three-dimensional space. This technique can be used to measure the grain-specific lattice (elastic) strain tensors, crystallographic orientations, centroids and volumes within bulk specimens ($\sim$1 mm^3) all in three dimensions (Pagan & Miller, 2014; Miller & Dawson, 2014; Schuren *et al.*, 2015).

Challenges from Bragg reflection overlap (also known as 'spot overlap') in ff-HEDM are not unique to SMAs. Several approaches are being developed to address this problem in ff-HEDM, including (i) improved preprocessing algorithms to better deconvolute overlapping reflections from the detector images (Sharma *et al.*, 2016), (ii) forward modeling diffraction through virtual microstructures to create virtual diffraction patterns, which are then statistically compared with the experimental patterns (Pagan & Miller, 2014; Wong *et al.*, 2013), and (iii) annealing the samples to a state where they have large, deformation-free grains and crystals that may give rise to larger deformed domains that are easier to observe directly (Paranjape *et al.*, 2017; Sedmák *et al.*, 2016; Pagan *et al.*, 2017).

APPENDIX C
CTM-based algorithm details

C1. Algorithm structure overview

Fig. 14 shows the general framework for the CTM-based forward model algorithm for using a ff-HEDM data set to identify martensite microstructures that formed from an initially austenite microstructure. To generate the HEDM

inputs for the algorithm, the austenite microstructure is completely analyzed with ff-HEDM software [*e.g. FABLE* (Schmidt, 2014), *HEXRD* (Bernier *et al.*, 2011) or *MIDAS* (Sharma *et al.*, 2016)] to determine the unstrained lattice parameters and crystallographic orientations for each crystal in the sample. The austenite analysis can either be performed (i) on the initial, unloaded sample, and the unstrained austenite lattice parameters can be used, or (ii) on the loaded sample where the austenite grain is within the elastic regime, and the strained austenite lattice parameters can be used. If it is also possible to measure the austenite grain center-of-mass position, then this position in the virtual sample should be used when forward modeling the martensite microstructures. The transformation work is calculated for each possible martensite microstructure; this calculation (discussed in the next section) requires the austenite stress state. If the austenite ff-HEDM analysis is being performed for an elastically loaded austenite grain, then the crystal stress state may be used. Otherwise, the macroscopic stress state can be used.

The possible martensite microstructures (*i.e.* martensite orientations, habit plane, shape strain direction, twin plane, shear direction and twin phase fractions) that could form from each crystal are then calculated according to the CTM using these inputs (a detailed explanation of these calculations follows in Appendix *C*2). Using all of the same experimental setup parameters as the actual experiment (*e.g.* X-ray energy, detector position, detector tilts *etc.*), the martensite orientations are then forward modeled through each of the possible martensite microstructures, producing a virtual diffraction pattern. Next, the virtual martensite diffraction pattern is statistically compared with the experimental martensite pattern, and the martensite microstructure that produces the virtual diffraction pattern that is closest to the experimental diffraction pattern is the identified martensite microstructure. In this article, we use the following procedure.

In the experimental diffraction patterns, the martensite Bragg reflection centroids (x and y location on the detector, and the sample rotation frame ω) are identified from the deformed sample measurements for some user-defined choice of (hkl) rings. This can be done manually or using the 'spot indexing' feature of a ff-HEDM software, though complete analyses of the martensite data are not necessary. The reflection centroid locations are also calculated for each virtual diffraction pattern. The actual martensite microstructure that formed under deformation is then identified by finding the smallest difference between the virtual and experimental reflection locations. The detector (x, y and ω) coordinates have a relative scaling that is sensitive to the detector size, the detector pixel size and the ω rotation increments chosen for the experiment. To equally weight the absolute differences between experimental and virtual reflections, reflection centroids are converted from their detector (x, y and ω) coordinates to the (χ, θ and η) coordinates of a unit pole figure, which are equally weighted, using the procedure described by Schuren & Miller (2011), Pagan & Miller (2016). Using these pole figure coordinates, the Euclidean distance between a virtual reflection centroid and an experimental reflection centroid is calculated and used as the metric for reflection distance comparisons. More specifically, the sum of the minimum Euclidean distances between all of the virtual and experimental reflections for a given crystallite (or pairs of martensite CV crystallites if making HPV
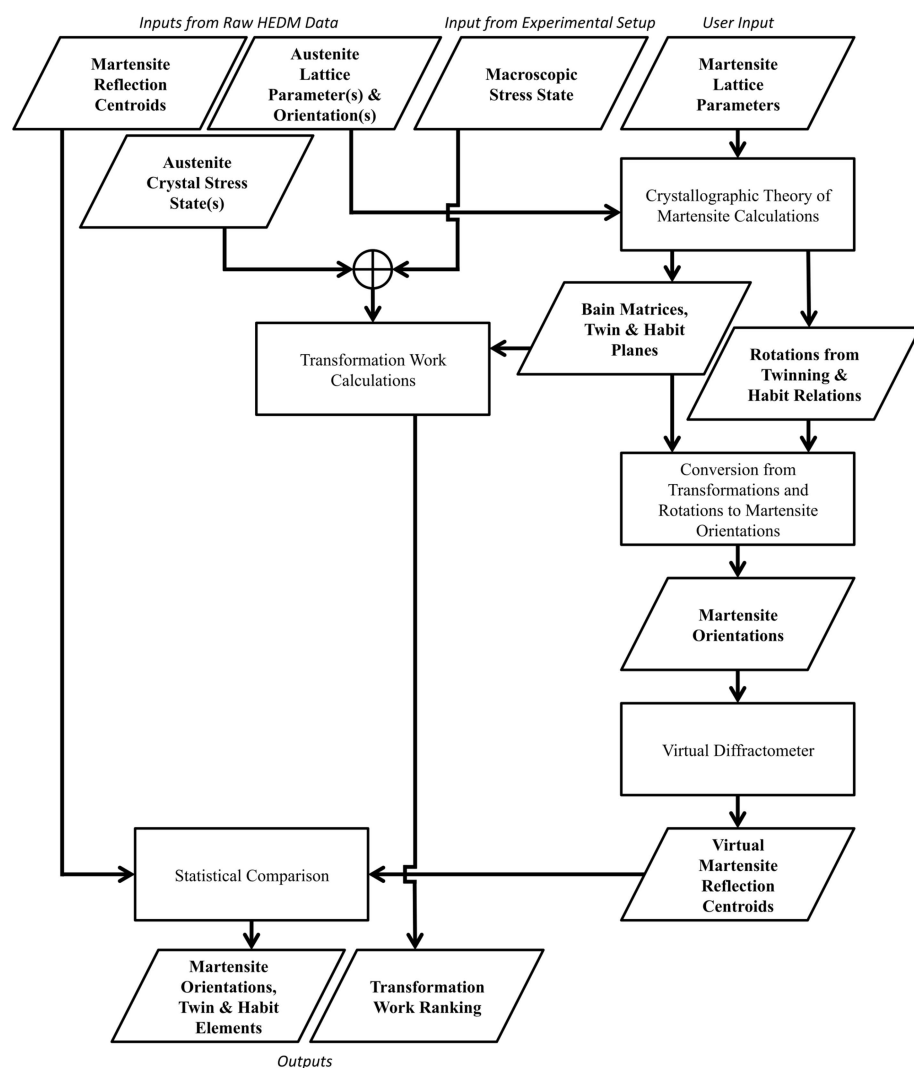

Figure 14
A flow chart showing the CTM-based forward model algorithm for ff-HEDM data analysis of martensite microstructures.

calculations, as we do in this work) for all of the user-defined (hkl) rings is computed. We use the term $\| \text{VD} - \text{ED} \|$ to indicate the total Euclidean distances between virtual and experimental Bragg reflections.

C2. CTM-based calculation details

The CTM for calculating compatible austenite–martensite interfaces has been published many times (Wechsler *et al.*, 1953; Bilby & Crocker, 1965; Ball & James, 1987; Hane & Shield, 1999; Bhattacharya, 2003). Here, even though we are using the established CTM verbatim, we reintroduce many of the well established equations and conditions to present the forward modeling procedure as clearly as possible. Specifically, there are many potential points of confusion between the CTM calculations and experimental orientation measurements, and it is not possible to discuss these nuances in detail without the fundamental equations of the CTM. The following discussion walks through a demonstration for cubic-to-monoclinic-I transformation of a NiTi sample. We will refer to monoclinic I as simply monoclinic here. This procedure can be used for other martensitic transformations as well and becomes simpler in cases of higher-symmetry martensites.

C2.1. Transformation matrices. The fundamental components of the CTM calculations are the transformation matrices, usually approximated as the Bain matrices, which are the pure stretch components of the deformation gradient between the austenite lattice and the martensite lattice. The transformation stretches γ, ε, α and δ that make up the transformation matrices, $\mathbf{U}_i$, are calculated directly from the austenite and martensite lattice parameters according to Bhattacharya (2003, p. 53–55) [or according to Hane & Shield (1999), using different symbols]. The subscript i is used to indicate the martensite CV, where the number of CVs is equal to the number of symmetries in the austenite point group divided by the number of symmetries in the martensite point group (Bhattacharya, 2003). For cubic-to-monoclinic transformations, there are 12 CVs, each with its own unique transformation matrix, $\mathbf{U}_1, \ldots, \mathbf{U}_{12}$.

Cubic-to-monoclinic transformation matrices are defined using the tetragonal representation of the cubic lattice, as this description of the transformation properly describes the volume change of the transformation. The full transformation from the cubic lattice to the monoclinic lattice is given in equation (1), where $\mathbf{c}_{1,2,3}$ are the cubic lattice vectors in the traditional cubic representation defined in standard crystallography texts (Nye, 1985), $\mathbf{m}'_{1,2,3}$ are the monoclinic lattice vectors and $\mathbf{Q}\mathbf{U}_i\mathbf{R}_{45}\mathbf{T}$ is the complete transformation from cubic to monoclinic. (Dot products are implied when two tensors are next to each other or when a vector is next to a tensor.) This complete transformation is comprised of $\mathbf{R}_{45}\mathbf{T}$, the transformation that converts the cubic representation of the cubic lattice vectors to the tetragonal representation, and $\mathbf{Q}\mathbf{U}_i$, the phase transformation from the tetragonally described cubic lattice to the monoclinic lattice. Each operation of the entire transformation is illustrated sequentially in Fig. 15: $\mathbf{T}$ stretches the primitive lattice vectors of the cubic

lattice into the correct tetragonal lattice vector lengths (Fig. 15a); $\mathbf{R}_{45}$ correctly orients the tetragonal representation by rotating the stretched cubic lattice 45° about the cubic lattice vector that has the same length as both the cubic and tetragonal representations (Fig. 15b); $\mathbf{U}_i$ applies the pure (Bain) stretch of the phase transformation from the tetragonally described cubic lattice to the monoclinic lattice (Fig. 15c); $\mathbf{Q}$ applies an additional small rotation that accompanies the stretch during the phase transformation (Fig. 15d). $\mathbf{Q}$ is the same for all CVs. This transformation is commonly reported in most discussions of cubic-to-monoclinic transformation calculations (Bhattacharya, 2003; Hane & Shield, 1999).

One nuance that is not commonly discussed but is critical to calculate the correct martensite microstructures for forward modeling is that different CVs require different tetragonal representations of the cubic lattice. For CVs 1–4 [following the numbering convention of Bhattacharya (2003, p. 55)], the cubic-to-tetragonal transformation is given by equation (2). For CVs 5–8 the transformation is given by equation (3). For CVs 9–12 the transformation is given by equation (4).

C2.2. Twin elements. The twin elements are the unknowns in the twinning equation in equation (5). This equation describes the compatible interface between two martensite variants i and j. This interface is called the twin plane, denoted by the vector normal to the plane $\hat{\mathbf{n}}$. The lattices on either side of the twin plane are related through a simple shear deformation of the lattice on one side of the twin plane in the direction of the vector $\mathbf{a}$ by a magnitude equal to the length of $\mathbf{a}$; hence, $\mathbf{a}$ is the twinning shear vector. Note the extra rotation, $\mathbf{R}$, that is required to satisfy the twin relation. In most references, including this article, this rotation is applied to $\mathbf{U}_i$.

All possible variant pairs i–j do not form compatible interfaces with each other – that is, only some of them satisfy the twinning equation, equation (5). A list of pairs that have solutions to the twinning equation can be found on p. 28 of Hane & Shield (1999). The twin element calculations are most computationally straightforward using the eigenvalue approach found in the work of Hane & Shield (1999) or Ball & James (1987), where the sorted eigenvalues of the symmetric matrix $\mathbf{C}_{ij} = \mathbf{U}_j^{-1}\mathbf{U}_i^2\mathbf{U}_j^{-1}$ are used to calculate $\mathbf{a}$ and $\hat{\mathbf{n}}$. The necessary extra rotation can then be calculated using equation (6). For each twin pair that satisfies the twinning equation, there are two possible solutions referred to as type I and type II twins, denoted as $\mathbf{a}^{\text{I}}$, $\hat{\mathbf{n}}^{\text{I}}$, $\mathbf{R}^{\text{I}}$ and $\mathbf{a}^{\text{II}}$, $\hat{\mathbf{n}}^{\text{II}}$, $\mathbf{R}^{\text{II}}$, respectively.

C2.3. Habit elements. The habit elements are the unknowns in what is commonly referred to as the habit plane equation in
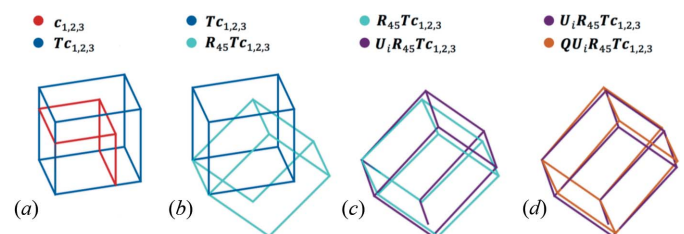

Figure 15
The sequence of transformations for calculating the transformed monoclinic lattice representation from the initial cubic lattice vectors.

equation (7), where $\mathbf{I}$ is the second-order identity tensor. According to the CTM, the austenite and martensite phases are only compatible if the middle eigenvalue of the transformation matrices is equal to 1 ($\lambda_{\mathrm{II}} = 1$; it will be the same for all $\mathbf{U}_i$) (Ball & James, 1987). For almost all SMAs, this condition is not satisfied, and the austenite and martensite phases are not perfectly compatible. The martensite can approximate compatibility through an average deformation formed by a twin pair i–j, where variants i and j have relative volume fractions f and $(1-f)$, respectively. The twin pair that satisfies the habit plane equation is called an HPV. The habit plane equation describes the 'approximately compatible' interface that forms between the austenite and the twinned martensite microstructures. This interface, called the habit plane, has a normal $\hat{\mathbf{m}}$, and the vector $\mathbf{b}$ is called the shape strain. The habit plane components can be calculated using a similar eigenvalue approach as was performed for the twin elements. This approach is based upon propositions of Ball & James (1987) and can be found in the work of both Hane & Shield (1999) and Bhattacharya (2003). Note the added rotation $\hat{\mathbf{R}}$ that must be applied to the twinned martensite microstructure. This extra necessary rotation, which will be applied to $\mathbf{U}_j$ and $\mathbf{RU}_i$, can then be calculated using equation (8). For each twin pair that satisfies the twinning equation, there are up to four possible habit plane solutions, denoted as $\mathbf{b}^{\mathrm{I-}}, \hat{\mathbf{m}}^{\mathrm{I-}}, \hat{\mathbf{R}}^{\mathrm{I-}}, \mathbf{b}^{\mathrm{I+}}, \hat{\mathbf{m}}^{\mathrm{I+}}, \mathbf{R}^{\mathrm{I+}}, \mathbf{b}^{\mathrm{II-}}, \hat{\mathbf{m}}^{\mathrm{II-}}, \hat{\mathbf{R}}^{\mathrm{II-}}$ and $\mathbf{b}^{\mathrm{II+}}, \hat{\mathbf{m}}^{\mathrm{II+}}, \hat{\mathbf{R}}^{\mathrm{II+}}$. (Not all possible twin pairs will have a solution to the habit plane equation.)

The notation used to describe HPV types in this article is the same as that used by Ball & James (1987), Bhattacharya (2003), Hane & Shield (1999), where I or II refers to a rational twin plane or a rational twinning shear direction, respectively, and (+) or (−) refers to the sign of the constant κ as defined by, *e.g.*, Hane & Shield (1999), Bhattacharya (2003).

C2.4. Maximum transformation work criterion. The transformation twinning strain is the strain observed when an austenite crystal fully transforms to a martensite HPV (Bucsek *et al.*, 2016). Summarizing the derivations given by Stebner *et al.* (2013) and Bucsek *et al.* (2016), this strain can be calculated from the habit elements as follows. The deformation gradient $\mathbf{F}'$ that takes the austenite lattice to the twinned martensite lattice is a simple shear and can be defined as in equation (9), where, again, $\mathbf{b}$ is called the shape strain and $\hat{\mathbf{m}}$ is the habit plane normal (see Appendix C2.3). The habit elements are typically defined in the cubic orientation of the cubic basis (Hane & Shield, 1999), so this deformation is expressed in the cubic lattice frame, or the cubic crystal coordinate system in Fig. 13. To express $\mathbf{F}'$ relative to the laboratory coordinate system, a transformation from the crystal coordinate system to the laboratory coordinate system must be applied. In diffraction, this transformation is the measured cubic orientation $\mathbf{O}_A$ (Bernier *et al.*, 2011), so the transformation is given by equation (10). The transformation twinning strain can then be written in terms of the habit elements using equation (11). The transformation work, W, for some stress state, $\boldsymbol{\sigma}$, is then given by equation (12). The maximum transformation work criterion states that the HPV that produces the largest trans-

formation work is the most favorable and likeliest to form (James, 1986; Bhattacharya, 2003; Zhang *et al.*, 2000). For an alloy that has n possible HPVs, the maximum work criterion is given by equation (13). Note that, for cases of uniaxial tension, this degenerates to a criterion of producing the maximum strain in the loading direction.

C2.5. Orientation conversions. For each HPV, full descriptions of the martensite lattices on either side of the twin plane within the HPV can be found by combining equations (1), (6) and (8). For cubic-to-monoclinic transformations where the cubic lattice vectors are given by $\mathbf{c}_1 = a_0\{100\}$, $\mathbf{c}_2 = a_0\{010\}$, $\mathbf{c}_3 = a_0\{001\}$, the martensite lattice description that results is shown in equation (14). Notice that the small rotation $\mathbf{Q}$ from equation (1) is not included. This is because the twin and habit relations were formed using only the pure stretch (Bain) matrices; thus, the rotations $\hat{\mathbf{R}}$ and $\mathbf{R}$ were derived using only the Bain matrices. It is important to use the appropriate $\mathbf{R}_{45}$ and $\mathbf{T}$ matrices depending on which CVs are present, as dictated by equations (2)–(4).

At this point, the monoclinic lattice descriptions resulting from equation (14), $\mathbf{m}'_{1,2,3}$, do not necessarily follow a conventional monoclinic lattice vector convention. For example, one common lattice vector convention for a monoclinic crystal system is $\mathbf{m}_1 = a\{100\}$, $\mathbf{m}_2 = b\{010\}$, $\mathbf{m}_3 = c\{\cos\beta\,0\,\sin\beta\}$, where $a < b < c$ and $\beta \neq 90°$. The deformations $\hat{\mathbf{R}}\mathbf{RU}_i$ and $\hat{\mathbf{R}}\mathbf{U}_j$ might transform the lattice vectors so that, for example, $\|\mathbf{m}'_1\| > \|\mathbf{m}'_2\|$ or $\mathbf{m}'_3 = -c(\cos\beta\,0\,\sin\beta)$. In other words, these descriptions accurately describe the lattice, but do not construct the lattice vectors in a way that is crystallographically conventional. The following procedure outlines how to convert the martensite lattice descriptions $\mathbf{m}'_1, \mathbf{m}'_2, \mathbf{m}'_3$ to a standard crystallographic lattice vector system $\mathbf{m}_1, \mathbf{m}_2, \mathbf{m}_3$, assuming all of the twin and habit elements have already been calculated.

A martensite lattice description, $\mathbf{m}'_1, \mathbf{m}'_2, \mathbf{m}'_3$, resulting from applying equation (14) can be converted to a conventional orientation, $\mathbf{O}$, with a series of three 'fixes'. Several such transformations could be derived; here we chose the one that was most logical in our work. The first step is to check the ordering of vector magnitudes and, if required, reorder them so that $\|\mathbf{m}'_1\| < \|\mathbf{m}'_2\| < \|\mathbf{m}'_3\|$. The second step is to check the sign of the angle between $\mathbf{m}'_1$ and $\mathbf{m}'_3$ and, if required, reverse the direction of $\mathbf{m}'_3$ (*i.e.* $\mathbf{m}'_3 = -\mathbf{m}'_3$) so that $\cos^{-1}[(\mathbf{m}'_1 \cdot \mathbf{m}'_3)/\|\mathbf{m}'_1\|\|\mathbf{m}'_3\|] = 90°$. The monoclinic orientation, $\mathbf{O}_M$, can now be calculated as the rotation component of the deformation that takes the conventional lattice vectors $\mathbf{m}_1, \mathbf{m}_2, \mathbf{m}_3$ to the calculated lattice description $\mathbf{m}'_1, \mathbf{m}'_2, \mathbf{m}'_3$. This can be done through polar decomposition [equations (15) and (16)], where $\mathbf{F}$ must be converted to principal component form to perform equation (16). The third and final step is to check the determinant of $\mathbf{O}_M$ and, if required, remove any inversion from the operation. In other words, if $\det(\mathbf{O}_M) = -1$, set $\mathbf{O}_M = -\mathbf{O}_M$ such that $\det(\mathbf{O}_M) = +1$. This must be done for both CVs i and j for each HPV pair. The resulting orientations do not change atomic positions but are now written with respect to the conventional monoclinic lattice vector choices for monoclinic space groups.

C3. Unique HPV orientations

For the cubic-to-monoclinic transformation in NiTi, there are 192 theoretically possible HPVs. Each of these HPVs results in two monoclinic CV orientations (384 total CV orientations). These orientations are unique with respect to each HPV. In other words, the two monoclinic orientations that occur in one HPV do not occur together in any other HPV. The uniqueness of the CV orientations within each HPV is shown in the pole figures of Fig. 16. The poles are colored so that blue corresponds to the ith orientation in an HPV and orange corresponds to the jth. Although many of these orientations appear to be closely oriented, they are sufficiently distinct by diffraction measures. In this example, the most closely oriented orientations are misoriented by 0.5°. Most ff-HEDM analyses can distinguish crystallite orientations within an uncertainty of approximately 0.01°, though these will be functions of the instrumentation, the choices made in data collection resolution, the calibration measurement and analysis software options (Bernier *et al.*, 2011; Oddershede *et al.*, 2010; Sharma *et al.*, 2012). In the cases where it is not possible to statistically distinguish between two HPV solutions, correlating the added criteria of relative twin volume fractions f and $(1 - f)$ with the intensities (volumes) of the grains in the ff-HEDM data will assist in uniquely identifying the correct HPV. This is demonstrated in the main body of the article. It is possible that for higher-symmetry martensites, or even different materials, this could be an issue in applying our forward model, so one must check these numbers carefully in studying other materials.

C4. Equations

$$\mathbf{m}'_{1,2,3} = \mathbf{Q}\mathbf{U}_i\mathbf{R}_{45}\mathbf{T}\mathbf{c}_{1,2,3} \tag{1}$$

$$\mathbf{R}_{45} = \begin{pmatrix} 1 & 0 & 0 \\ 0 & 2^{1/2} & 2^{1/2} \\ 0 & -2^{1/2} & 2^{1/2} \end{pmatrix}, \quad \mathbf{T} = \begin{pmatrix} 1 & 0 & 0 \\ 0 & 2^{1/2} & 0 \\ 0 & 0 & 2^{1/2} \end{pmatrix} \tag{2}$$

$$\mathbf{R}_{45} = \begin{pmatrix} 2^{1/2} & 0 & -2^{1/2} \\ 0 & 1 & 0 \\ 2^{1/2} & 0 & 2^{1/2} \end{pmatrix}, \quad \mathbf{T} = \begin{pmatrix} 2^{1/2} & 0 & 0 \\ 0 & 1 & 0 \\ 0 & 0 & 2^{1/2} \end{pmatrix} \tag{3}$$

$$\mathbf{R}_{45} = \begin{pmatrix} 2^{1/2} & 2^{1/2} & 0 \\ -2^{1/2} & 2^{1/2} & 0 \\ 0 & 0 & 1 \end{pmatrix}, \quad \mathbf{T} = \begin{pmatrix} 2^{1/2} & 0 & 0 \\ 0 & 2^{1/2} & 0 \\ 0 & 0 & 1 \end{pmatrix} \tag{4}$$

$$\mathbf{R}\mathbf{U}_i - \mathbf{U}_j = \mathbf{a} \otimes \hat{\mathbf{n}} \tag{5}$$

$$\mathbf{R} = (\mathbf{a} \otimes \hat{\mathbf{n}} + \mathbf{U}_j)\mathbf{U}_i^{-1} \tag{6}$$

$$\hat{\mathbf{R}}[f\mathbf{R}\mathbf{U}_i + (1 - f)\mathbf{U}_j] - \mathbf{I} = \mathbf{b} \otimes \hat{\mathbf{m}} \tag{7}$$

$$\hat{\mathbf{R}} = (\mathbf{b} \otimes \hat{\mathbf{m}} + \mathbf{I})[f\mathbf{R}\mathbf{U}_i + (1 - f)\mathbf{U}_j]^{-1} \tag{8}$$

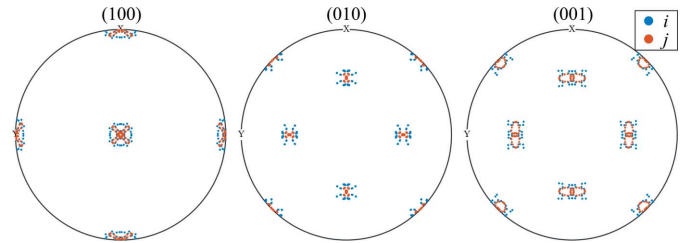$$\mathbf{F}' = \mathbf{I} + \mathbf{b} \otimes \hat{\mathbf{m}} \tag{9}$$

Figure 16
Pole figures showing the 384 orientations that arise in HPVs that are unique because of the small rotations in the twinning and habit equations. Blue corresponds to CV i and orange corresponds to CV j.

$$\mathbf{F} = \mathbf{O}_A\mathbf{F}'\mathbf{O}_A^{\mathrm{T}} \tag{10}$$

$$\varepsilon^{\mathrm{transf}} = \frac{1}{2}(\mathbf{F}^{\mathrm{T}}\mathbf{F} - \mathbf{I}) \tag{11}$$

$$W = \boldsymbol{\sigma} : \boldsymbol{\varepsilon}^{\mathrm{transf}} \tag{12}$$

$$\max_{i=1,\ldots n} \boldsymbol{\sigma} : \boldsymbol{\varepsilon}_i^{\mathrm{transf}} = \max_{i=1,\ldots n} \hat{\boldsymbol{\sigma}} : \boldsymbol{\varepsilon}_i^{\mathrm{transf}} \tag{13}$$

$$\mathbf{m}'_{1,2,3_i} = \hat{\mathbf{R}}\mathbf{R}\mathbf{U}_i\mathbf{R}_{45}\mathbf{T}\mathbf{c}_{1,2,3}, \quad \mathbf{m}'_{1,2,3_j} = \hat{\mathbf{R}}\mathbf{U}_j\mathbf{R}_{45}\mathbf{T}\mathbf{c}_{1,2,3} \tag{14}$$

$$\mathbf{F} = (\mathbf{m}'_1 \ \mathbf{m}'_2 \ \mathbf{m}'_3)(\mathbf{m}_1 \ \mathbf{m}_2 \ \mathbf{m}_3)^{-1} \tag{15}$$

$$\mathbf{U} = (\mathbf{F}^{\mathrm{T}}\mathbf{F})^{1/2}, \quad \mathbf{O}_{\mathrm{M}} = \mathbf{F}\mathbf{U}^{-1}. \tag{16}$$

References

Abdolvand, H., Majkut, M., Oddershede, J., Wright, J. P. & Daymond, M. R. (2015). *Acta Mater.* **93**, 235–245.
Abeyaratne, R. & Knowles, J. K. (1991). *Arch. Ration. Mech. Anal.* **114**, 119–154.
Aydiner, C. C., Bernier, J. V., Clausen, B., Lienert, U., Tome, C. N. & Brown, D. W. (2009). *Phys. Rev. B*, **80**, 024113.
Ball, J. M. & James, R. D. (1987). *Arch. Ration. Mech. Anal.* **100**, 13–52.
Barton, N. R. & Bernier, J. V. (2012). *J. Appl. Cryst.* **45**, 1145–1155.

Bernier, J. V., Barton, N. R., Lienert, U. & Miller, M. P. (2011). *J. Strain Anal. Eng. Des.* **46**, 527–547.

Berveiller, S., Malard, B., Wright, J., Patoor, E. & Geandier, G. (2011). *Acta Mater.* **59**, 3636–3645.

Bhattacharya, K. (2003). *Microstructure of Martensite: Why it Forms and How it Gives Rise to the Shape Memory Effect.* Oxford University Press.

Bilby, B. & Crocker, A. (1965). *Proc. R. Soc. London A Math. Phys. Eng. Sci.* **288**, 240–255.

Blaber, J., Adair, B. & Antoniou, A. (2015). *Exp. Mech.* **55**, 1105–1122.

Bowles, J. S. & Mackenzie, J. K. (1954). *Acta Metall.* **2**, 129–137.

Bucsek, A. N., Hudish, G. A., Bigelow, G. S., Noebe, R. D. & Stebner, A. P. (2016). *Shape Mem. Superelasticity*, **2**, 62–79.

Buhrer, W., Gotthardt, R., Kulik, A., Mercier, O. & Staub, F. (1983). *J. Phys. F Met. Phys.* **13**, L77–L81.

Chen, X., Srivastava, V., Dabade, V. & James, R. D. (2013). *J. Mech. Phys. Solids*, **61**, 2566–2587.

Chu, C. H. (1993). *Hysteresis and Microstructures: A Study of Biaxial Loading on Compound Twins of Copper–Aluminum–Nickel Single Crystals.* University of Minnesota, USA.

Coughlin, D. R., Phillips, P. J., Bigelow, G. S., Garg, A., Noebe, R. D. & Mills, M. J. (2012). *Scr. Mater.* **67**, 112–115.

Duerig, T. W., Melton, K. N., Stockel, D. & Wayman, C. M. (1990). *Engineering Aspects of Shape Memory Alloys.* Boston: Butterworth-Heinemann.

Dunand, D. C., Mari, D., Bourke, M. & Roberts, J. A. (1996). *Metall. Mater. Trans. A*, **27**, 2820–2836.

Gall, K., Dunn, M. L., Liu, Y., Labossiere, P., Sehitoglu, H. & Chumlyakov, Y. I. (2002). *J. Eng. Mater. Technol.* **124**, 238–245.

Gotz, A., Suchet, G. & Evan, K. (2007). *FABLE.* http://sourceforge.net/p/fable/wiki/Home/

Gupta, S. P. & Johnson, A. A. (1973). *Trans. JIM*, **14**, 292–302.

Hane, K. F. & Shield, T. W. (1998). *Philos. Mag. A*, **78**, 1215–1252.

Hane, K. F. & Shield, T. (1999). *Acta Mater.* **47**, 2603–2617.

Henrie, B. L., Mason, T. A. & Bingert, J. F. (2005). *Mater. Sci. Forum*, **495**, 191–196.

Hornbuckle, B. C., Yu, X. X., Noebe, R. D., Martens, R., Weaver, M. L. & Thompson, G. B. (2015). *Mater. Sci. Eng. A*, **639**, 336–344.

Inamura, T., Nishiura, T., Kawano, H., Hosoda, H. & Nishida, M. (2012). *Philos. Mag.* **92**, 2247–2263.

James, R. D. (1986). *J. Mech. Phys. Solids*, **34**, 359–394.

Khalil-Allafi, J., Schmahl, W. W., Wagner, M., Sitepu, H., Toebbens, D. M. & Eggeler, G. (2004). *Mater. Sci. Eng. A*, **378**, 161–164.

Kim, Y., Ahn, T.-H., Suh, D.-W. & Han, H. N. (2015). *Scr. Mater.* **104**, 13–16.

Kimiecik, M., Jones, J. W. & Daly, S. (2013). *Mater. Lett.* **95**, 25–29.

Kimiecik, M., Jones, J. W. & Daly, S. (2016). *J. Mech. Phys. Solids*, **89**, 16–30.

Laplanche, G., Birk, T., Schneider, S., Frenzel, J. & Eggeler, G. (2017). *Acta Mater.* **127**, 143–152.

Lauridsen, E. M., Schmidt, S., Suter, R. M. & Poulsen, H. F. (2001). *J. Appl. Cryst.* **34**, 744–750.

Li, Z. Q. (2002). *Int. J. Plast.* **18**, 1481–1498.

Lienert, U., Li, S. F., Hefferan, C. M., Lind, J., Suter, R. M., Bernier, J. V., Barton, N. R., Brandes, M. C., Mills, M. J., Miller, M. P., Jakobsen, B. & Pantleon, W. (2011). *JOM*, **63**, 70–77.

Lind, J., Li, S., Pokharel, R., Lienert, U., Rollett, A. & Suter, R. (2014). *Acta Mater.* **76**, 213–220.

Liu, D., Peterlechner, M., Fiebig, J., Trubel, S., Wegner, M., Du, Y., Jin, Z., Wilde, G. & Divinski, S. V. (2015). *Intermetallics*, **61**, 30–37.

Liu, Y., Xie, Z. L., Van Humbeeck, J. & Delaey, L. (1999). *Acta Mater.* **47**, 645–660.

Liu, Y., Xie, X. L., Van Humbeeck, J., Delaey, L. & Liu, Y. N. (2000). *Philos. Mag. A*, **80**, 1935–1953.

Madangopal, K. & Banerjee, R. (1992). *Scr. Metall. Mater.* **27**, 1627–1632.

Mercier, O., Melton, K. N., Gremaud, G. & Hägi, J. (1980). *J. Appl. Phys.* **51**, 1833–1834.

Miller, M. P. & Dawson, P. R. (2014). *Curr. Opin. Solid State Mater. Sci.* **18**, 286–299.

Miyazaki, S., Kimura, S., Otsuka, K. & Suzuki, Y. (1984). *Scr. Metall.* **18**, 883–888.

Ni, X., Greer, J. R., Bhattacharya, K., James, R. D. & Chen, X. (2016). *Nano Lett.* **16**, 7621–7625.

Nishida, M., Okunishi, E., Nishiura, T., Kawano, H., Inamura, T., Ii, S. & Hara, T. (2012). *Philos. Mag.* **92**, 2234–2246.

Nishida, M., Wayman, C. M. & Chiba, A. (1988). *Metallography*, **21**, 275–291.

Norfleet, D. M., Sarosi, P. M., Manchiraju, S., Wagner, M. F. X., Uchic, M. D., Anderson, P. M. & Mills, M. J. (2009). *Acta Mater.* **57**, 3549–3561.

Nye, J. F. (1985). *Physical Properties of Crystals: Their Representation by Tensors and Matrices.* New York: Oxford University Press.

Obstalecki, M., Wong, S. L., Dawson, P. R. & Miller, M. P. (2014). *Acta Mater.* **75**, 259–272.

Oddershede, J., Schmidt, S., Poulsen, H. F., Sørensen, H. O., Wright, J. & Reimers, W. (2010). *J. Appl. Cryst.* **43**, 539–549.

Onda, T., Bando, Y., Ohba, T. & Otsuka, K. (1992). *Mater. Trans. JIM*, **33**, 354–359.

Otsuka, K. & Ren, X. (2005). *Prog. Mater. Sci.* **50**, 511–678.

Otsuka, K., Sawamura, T. & Shimizu, K. (1971). *Phys. Status Solidi A*, **5**, 457–470.

Otsuka, K. & Wayman, C. M. (1998). *Shape Memory Materials.* Cambridge University Press.

Pagan, D. C. & Miller, M. P. (2014). *J. Appl. Cryst.* **47**, 887–898.

Pagan, D. C. & Miller, M. P. (2016). *Acta Mater.* **116**, 200–211.

Pagan, D. C., Shade, P. A., Barton, N. R., Park, J.-S., Kenesei, P., Menasche, D. B. & Bernier, J. V. (2017). *Acta Mater.* **128**, 406–417.

Paranjape, H. M., Manchiraju, S. & Anderson, P. M. (2016). *Int. J. Plast.* **80**, 1–18.

Paranjape, H. M., Paul, P. P., Amin-Ahmadi, B., Sharma, H., Dale, D., Ko, J. Y. P., Chumlyakov, Y. I., Brinson, L. C. & Stebner, A. P. (2018). *Acta Mater.* **144**, 748–757.

Paranjape, H. M., Paul, P. P., Sharma, H., Kenesei, P., Park, J.-S., Duerig, T. W., Brinson, L. C. & Stebner, A. P. (2017). *J. Mech. Phys. Solids*, **102**, 46–66.

Paul, P. P., Paranjape, H. M., Amin-Ahmadi, B., Stebner, A. P., Dunand, D. C. & Brinson, L. C. (2017). *Mater. Sci. Eng. A*, **706**, 227–235.

Poulsen, H. F. (2004). *Three-dimensional X-ray Diffraction Microscopy: Mapping Polycrystals and Their Dynamics.* Berlin: Springer.

Poulsen, H. F. (2012). *J. Appl. Cryst.* **45**, 1084–1097.

Poulsen, H. F., Nielsen, S. F., Lauridsen, E. M., Schmidt, S., Suter, R. M., Lienert, U., Margulies, L., Lorentzen, T. & Juul Jensen, D. (2001). *J. Appl. Cryst.* **34**, 751–756.

Schmidt, S. (2014). *J. Appl. Cryst.* **47**, 276–284.

Schuren, J. & Miller, M. (2011). *J. Strain Anal. Eng. Des.* **46**, 663–681.

Schuren, J. C., Shade, P. A., Bernier, J. V., Li, S. F., Blank, B., Lind, J., Kenesei, P., Lienert, U., Suter, R. M., Turner, T. J., Dimiduk, D. M. & Almer, J. (2015). *Curr. Opin. Solid State Mater. Sci.* **19**, 235–244.

Sedmák, P., Pilch, J., Heller, L., Kopeček, J., Wright, J., Sedlák, P., Frost, M. & Šittner, P. (2016). *Science*, **353**, 559–562.

Shade, P. A., Blank, B., Schuren, J. C., Turner, T. J., Kenesei, P., Goetze, K., Suter, R. M., Bernier, J. V., Li, S. F., Lind, J., Lienert, U. & Almer, J. (2015). *Rev. Sci. Instrum.* **86**, 093902.

Sharma, H., Almer, J., Park, J.-S., Kenesei, P., Wilde, M. & Wozniak, J. (2016). *MIDAS, Microstructural Imaging using Diffraction Analysis Software.* https://www.aps.anl.gov/Science/Scientific-Software/MIDAS

Sharma, H., Huizenga, R. M. & Offerman, S. E. (2012). *J. Appl. Cryst.* **45**, 705–718.

Shaw, J. A. (2000). *Int. J. Plast.* **16**, 541–562.

Shield, T. W. (1995). *J. Mech. Phys. Solids*, **43**, 869–895.

Simons, H., Jakobsen, A. C., Ahl, S. R., Detlefs, C. & Poulsen, H. F. (2016). *MRS Bull.* **41**, 454–459.

Simons, H., King, A., Ludwig, W., Detlefs, C., Pantleon, W., Schmidt, S., Stöhr, F., Snigireva, I., Snigirev, A. & Poulsen, H. F. (2015). *Nat. Commun.* **6**, 6098.

Šittner, P., Lukáš, P., Novák, V., Daymond, M. R. & Swallowe, G. M. (2004). *Mater. Sci. Eng. A*, **378**, 97–104.

Šittner, P. & Novák, V. (2004). *Scr. Mater.* **51**, 321–326.

Song, Y., Chen, X., Dabade, V., Shield, T. W. & James, R. D. (2013). *Nature*, **502**, 85–88.

Stebner, A., Vogel, S., Noebe, R., Sisneros, T., Clausen, B., Brown, D., Garg, A. & Brinson, L. (2013). *J. Mech. Phys. Solids*, **61**, 2302–2330.

Turner, T. J., Shade, P. A., Bernier, J. V., Li, S. F., Schuren, J. C., Lind, J., Lienert, U., Kenesei, P., Suter, R. M., Blank, B. & Almer, J. (2016). *Integr. Mater. Manuf. Innov.* **5**, 5.

Wechsler, M. S., Lieberman, D. S. & Read, T. A. (1953). *Trans. AIME*, **197**, 1503–1515.

Wong, S. L., Park, J.-S., Miller, M. P. & Dawson, P. R. (2013). *Comput. Mater. Sci.* **77**, 456–466.

Zhang, X. Y., Brinson, L. C. & Sun, Q. P. (2000). *Smart Mater. Struct.* **9**, 571–581.